

Study of Pressure Effect on the Au-Al-Yb  
Quasicrystal and its Approximant Crystal  
(Au-Al-Yb 準結晶及び近似結晶に対する  
圧力効果の研究)

Shuya MATSUKAWA

松川 周矢



# Contents

<b>1</b>	<b>Introduction</b>	<b>3</b>
1.1	Background . . . . .	3
1.2	Quasicrystals . . . . .	4
1.2.1	Structural properties . . . . .	6
1.3	Heavy fermions . . . . .	11
1.3.1	Quantum critical phenomena . . . . .	13
1.4	Au-Al-Yb quasicrystal and approximant . . . . .	14
1.4.1	Structure model . . . . .	14
1.4.2	Physical properties . . . . .	16
1.5	Purposes of this thesis . . . . .	23
<b>2</b>	<b>Pressure Effect on Quantum Criticality of the Au-Al-Yb Quasicrystal</b>	<b>25</b>
2.1	Introduction . . . . .	25
2.2	Experimental Method . . . . .	25
2.3	Results and Discussion . . . . .	26
2.3.1	Dc magnetization of the Au-Al-Yb quasicrystal under hydrostatic pressure . . . . .	26
2.3.2	Calibration method of ac magnetic susceptibility under pressure . . . . .	28
2.3.3	Magnetic susceptibility of the Au-Al-Yb quasicrystal under hydrostatic pressure . . . . .	28
2.3.4	Electrical resistivity of the Au-Al-Yb quasicrystal under hydrostatic pressure . . . . .	30
2.3.5	Origin of the robustness of the pressure effect . . . . .	30
2.4	Summary . . . . .	30
<b>3</b>	<b>Pressure-Driven Quantum Criticality in the Au-Al-Yb Approximant</b>	<b>33</b>
3.1	Introduction . . . . .	33
3.2	Experimental Method . . . . .	33

3.3	Results and Discussion . . . . .	34
3.3.1	Electrical resistivity of the Au-Al-Yb approximant under hydrostatic pressure . . . . .	34
3.3.2	Dc magnetization under pressure . . . . .	35
3.3.3	Magnetic susceptibility of the Au-Al-Yb approximant under hydrostatic pressure . . . . .	35
3.3.4	Nature of the magnetic ordered phase above 2 GPa: an antiferromagnetically long-range ordered phase or a spin glass like short-range ordered phase . . . . .	37
3.3.5	Origin of the quantum criticality of the Au-Al-Yb approximant . . . . .	41
3.3.6	$P$ - $T$ phase diagram of the Au-Al-Yb approximant . . . . .	42
3.3.7	Chemical pressure effect on the Au-Al-Yb approximant: valence change driven by constituent element substitution . . . . .	43
3.4	Summary . . . . .	44
<b>4</b>	<b>Discussion</b> . . . . .	<b>45</b>
4.1	Introduction . . . . .	45
4.2	Origin of the difference in the pressure effect between the Au-Al-Yb quasicrystal and the approximant . . . . .	45
4.3	$T/H$ scaling of the Au-Al-Yb quasicrystal and the approximant . . . . .	46
4.4	Origin of the unusual quantum criticality . . . . .	50
4.5	Summary . . . . .	51
<b>5</b>	<b>Summary</b> . . . . .	<b>55</b>

# Chapter 1

## Introduction

### 1.1 Background

It is well known that every solid belongs to crystals, amorphous alloys, or quasicrystals. The atomic arrangement is periodic in crystals and aperiodic in amorphous alloys. By contrast, quasicrystals have quasiperiodic structure (see section 1.2.1). Reflecting this long-range ordered nature, quasicrystals show sharp Bragg reflection patterns like crystals. In contrast to conventional crystals, however, they have rotational symmetries forbidden to conventional crystals (for example, 5-, 8-, 10-fold symmetries). These interesting features of the geometric structure have fascinated many researchers, including physicists. So far, the electronic states unique to the quasicrystals have not been revealed yet. For example, it is not known if there is an exotic magnetic structure unique to quasicrystals. Theoretically, it was suggested that a “critical state” is formed due to the quasiperiodicity. However, this has not been proved experimentally. Recently, a new type of the quasicrystal, the Au-Al-Yb quasicrystal [1], was found in which the thermodynamic properties such as the magnetic susceptibility and the specific heat diverge as  $T \rightarrow 0$ , with the unusual critical indices [2]. Interestingly, these indices are found to be similar to those of heavy fermion crystals  $\text{YbRh}_2\text{Si}_2$  and  $\beta\text{-YbAlB}_4$  [3,4]. These findings allow us to expect that there is new physics in the interdisciplinary region between heavy fermions and quasicrystals.

In this thesis, we study the pressure effect on the quantum criticality of the novel Au-Al-Yb quasicrystal and its approximant crystal. Chapter 1 is devoted to introduction. In Chapter 2, we investigate the magnetic susceptibility of the Au-Al-Yb quasicrystal under hydrostatic pressure and show that the magnetic susceptibility diverges toward zero temperature under pressure, with the same critical index as the ambient pressure. This means that the quantum criticality survives under pressure in the quasicrystal and

the quantum criticality of the quasicrystal is robust against the application of hydrostatic pressure. This behavior is remarkably different from that of the conventional crystals. To reveal if this behavior is unique to the quasicrystal, we investigate the magnetic susceptibility of the approximant under hydrostatic pressure in Chapter 3. We show that the magnetic susceptibility strongly increases with pressure and diverges at the critical pressure  $P_c \sim 2$  GPa. This means that there is a quantum critical point at  $P_c$ . At  $P > P_c$ , we find that the spin-glass-like short-range ordered state emerges below the freezing temperature  $T_g \sim 100$  mK. We note that this does not mean that  $P_c$  corresponds to a magnetic quantum critical point. In Chapter 4, we compare the Au-Al-Yb quasicrystal with the approximant, and discuss the origin of the quantum criticality of them. The difference between the quasicrystal and approximant is the presence/absence of the quasiperiodicity. Therefore, the difference observed in the pressure effect can be ascribed to the difference in the presence/absence of the quasiperiodicity. For the further study of the origin of the quantum criticality, we examine the so-called  $T/H$  scaling. We find that the quasicrystal and the approximant satisfy the  $T/H$  scaling similar to  $\text{CeCu}_{6-x}\text{Au}_x$  and  $\beta\text{-YbAlB}_4$ . From this finding, we suggest that the mechanism of the novel quantum criticality is the same as that in these heavy fermion crystals. Finally, we give a brief summary in Chapter 5.

## 1.2 Quasicrystals

Quasicrystals are defined as follows:

- (i) Fourier transformation of the atomic arrangement consists of set of delta functions.
- (ii) The number of the basis vector is more than the dimension of the space.
- (iii) Quasicrystals show forbidden rotational symmetries to conventional crystals.

The point (i) means that the quasicrystals show the sharp diffraction peaks in reciprocal space and hence have the long-range ordered structure. Therefore, the quasicrystals are completely different from amorphous materials. Usually, the diffraction peaks of 3 dimensional crystals are indexed using three basis vectors. For the quasicrystals, the more than 3 basis vectors are needed. This gives the second definition. As shown below, this is directly deduced from the quasiperiodicity. The point (iii) suggests that the quasicrystals have rotational symmetries (for example, 5-, 8-, 10-fold symmetries) forbidden to conventional crystals.

There are quasicrystals classified as 2 dimensional and 3 dimensional quasicrystals. The 2 dimensional quasicrystals have two quasiperiodic axes

and one periodic axis: the planes which have quasiperiodic arrangement of atoms stack periodically for the direction of the periodic axis. The 3 dimensional quasicrystals show the quasiperiodicity for all the directions. These are icosahedral quasicrystals. The icosahedral quasicrystals have the symmetry of the icosahedron. Their structures consist of the atomic groups called clusters (see Fig. 1.1). The clusters are composed of the concentric arrangement of multiple shells. The quasicrystals have distinct multiple shells, which are known as Mackay-, Bergman-, and Tsai-type cluster (see Figs. 1.2-1.4). The cluster of the Au-Al-Yb quasicrystal, which is studied in this thesis, belongs to the Tsai-type [1]. We note that the approximant possesses the same local structure as the quasicrystal.

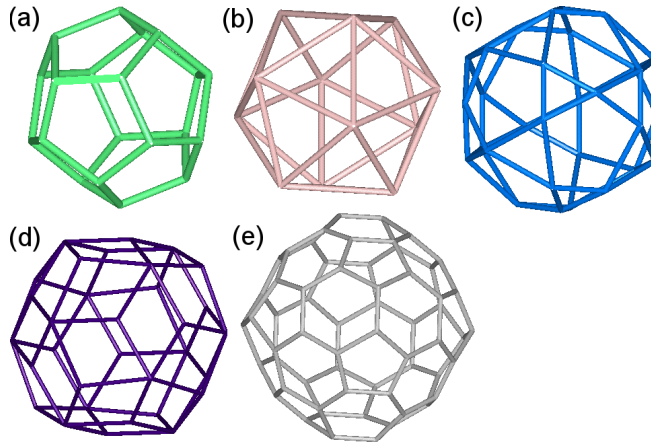


**Figure 1.1:** Illustration of polyhedrons which have the icosahedral symmetry. (a) Dodecahedron. (b) Icosahedron. (c) Icosidodecahedron. (d) Rhombic triacontahedron. (e) Truncated icosahedron.

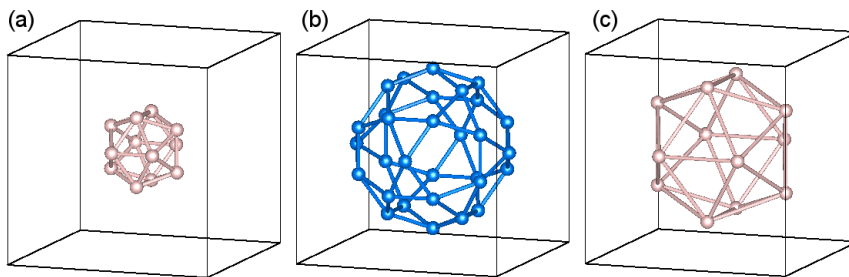


**Figure 1.2:** Illustration of Mackay-type cluster. The first shell is an icosahedron (a), the second shell is an icosidodecahedron (b), and the third shell is an icosahedron (c).

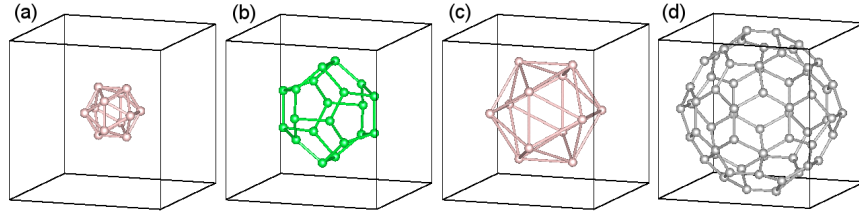


**Figure 1.3:** Illustration of Bergman-type cluster. The first shell is an icosahedron (a), the second shell is a dodecahedron (b), the third shell is an icosahedron (c), and the fourth shell is a truncated icosahedron (d).

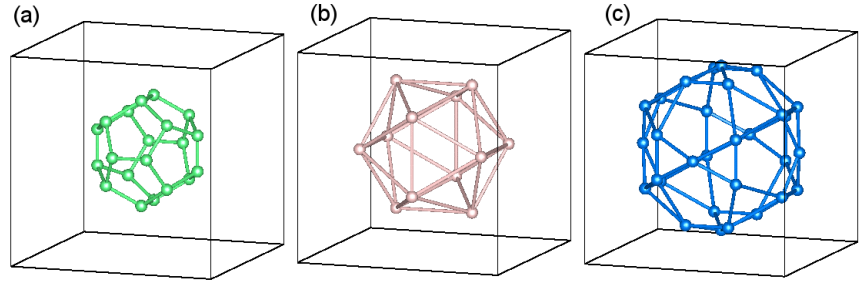


**Figure 1.4:** Illustration of Tsai-type cluster. The first shell is a dodecahedron (a), the second shell is an icosahedron (b), and the third shell is an icosidodecahedron (c).

### 1.2.1 Structural properties

#### Quasiperiodicity

First, we consider the quasiperiodicity. Quasiperiodicity is a kind of order, other than periodicity. One of such examples is the Fibonacci sequence, which is defined as follows:

$$A_0 = 0, \tag{1.1}$$

$$A_1 = 1, \tag{1.2}$$

$$A_N = A_{N-1} + A_{N-2} \quad (N \geq 2). \tag{1.3}$$

This gives the following Fibonacci sequence:

$$\{0, 1, 1, 2, 3, 5, 8, 13, \dots\}$$

The sequence may look to be random but is formed from the rules mentioned above (Eqs. 1.1~3). This is the quasiperiodicity. It is interesting to note

that  $A_N/A_{N+1}$  becomes equal to the golden ratio  $\tau$  in the limit of  $N \rightarrow \infty$ . Here,  $\tau$  is an irrational number,  $\frac{1+\sqrt{5}}{2}$ .

The Fibonacci sequence can be also related to the sequence of the word, S and L, defined as follows:

$$A_0 = S, \tag{1.4}$$

$$A_1 = L, \tag{1.5}$$

$$A_N = A_{N-1} + A_{N-2} \quad (N \geq 2). \tag{1.6}$$

This is expressed as follows,

$$N = 0 : S,$$

$$N = 1 : L,$$

$$N = 2 : LS,$$

$$N = 3 : LSL,$$

$$N = 4 : LSLLS,$$

$$N = 5 : LSLLSLSL,$$

. . . . .

. . . . .

. . . . .

Note that the number ratio of S to L becomes equal to  $\tau$  in the limit of  $N \rightarrow \infty$ .

### One dimensional quasiperiodic lattice

A projection method is one of the good methods which can describe quasiperiodic structures [5,6]. Specifically, the 3 dimensional quasiperiodic structure is obtained by projection from the 6 dimensional periodic structure. This means that the 3 dimensional quasiperiodic structure needs 6 basis vectors. Since the projection from the 6 dimensional periodic structure is very complex, we consider the 1 dimensional quasiperiodic lattice, which is obtained from the 2 dimensional periodic lattice.

First, let us consider the square lattice in the plane of  $X_1$  and  $X_2$  (see Fig. 1.5). The position vector  $\vec{r}$  of the square lattice is defined as follows by using integers  $n_1, n_2$  and the unit vectors  $\vec{E}_1, \vec{E}_2$ :

$$\vec{r} = a_{2D} \left( n_1 \vec{E}_1 + n_2 \vec{E}_2 \right). \tag{1.7}$$

Here,  $a_{2D}$  is the lattice constant of the square lattice. Next, let us separate the 2 dimension space into two orthogonal subspaces,  $X_{\parallel}$  (“physical space”) and  $X_{\perp}$  (“complementary space”), by rotating the original set of the axes

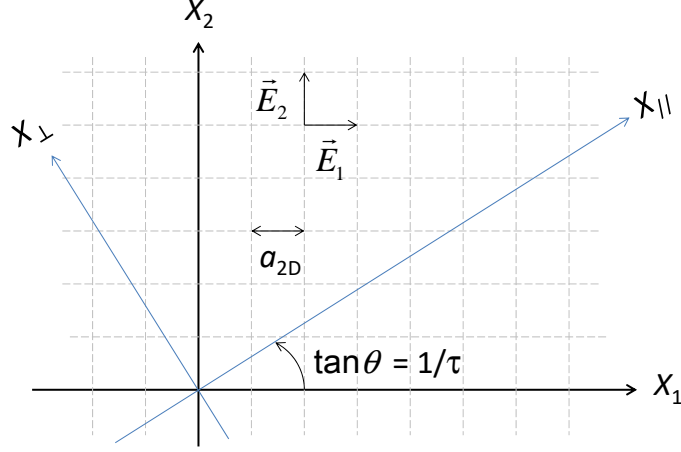


**Figure 1.5:** Construction of the periodic square lattice.  $X_1$  and  $X_2$  denote the square lattice.  $X_{\parallel}$  and  $X_{\perp}$  denote the physical space and the complementary space, respectively.  $\vec{E}_1$  and  $\vec{E}_2$  are the basis vectors of the 2 dimensional periodic lattice, respectively.

by some angle  $\theta$  such that  $\tan\theta = 1/\tau$  (where  $\tau = \frac{1+\sqrt{5}}{2}$  is the golden ratio). The 1 dimensional quasiperiodic lattice is obtained by projecting the 2 dimensional periodic lattice on  $X_{\parallel}$ . If all the lattice points are projected on  $X_{\parallel}$ ,  $X_{\parallel}$  is dense with the projected points and the 1 dimensional quasiperiodic lattice is not obtained. To limit projection, we define the confined region, which is called “window”. We define the “window length” as indicated in Fig. 1.6. Here, we set the slope  $\alpha$  of the window such that  $\alpha = \theta$ . Thus obtained 1 dimensional quasiperiodic lattice consists of two kinds of length, S (short) and L (long). The position vector  $\vec{r}_{\parallel}$  of this 1 dimensional quasiperiodic lattice is expressed as follows:

$$\vec{r}_{\parallel} = a_{2D} \left( n_1 \vec{E}_{1\parallel} + n_2 \vec{E}_{2\parallel} \right). \quad (1.8)$$

Here,  $\vec{E}_{1\parallel}$  and  $\vec{E}_{2\parallel}$  are the vectors obtained by projection from  $\vec{E}_1$  and  $\vec{E}_2$ , corresponding to L and S, respectively. These vectors are the basis vectors of the 1 dimensional quasiperiodic lattice. Therefore, we need two basis vectors to express the 1 dimensional quasiperiodic lattice. Note that the number ratio of S to L is  $\tau$ , again.

In the Fibonacci sequence, we define the ratio  $A_N/A_{N-1}$  of the adjacent numbers as follows:

$$1/1, 2/1, 3/2, 5/3, 8/5, \dots A_N/A_{N-1}, \dots \quad (1.9)$$

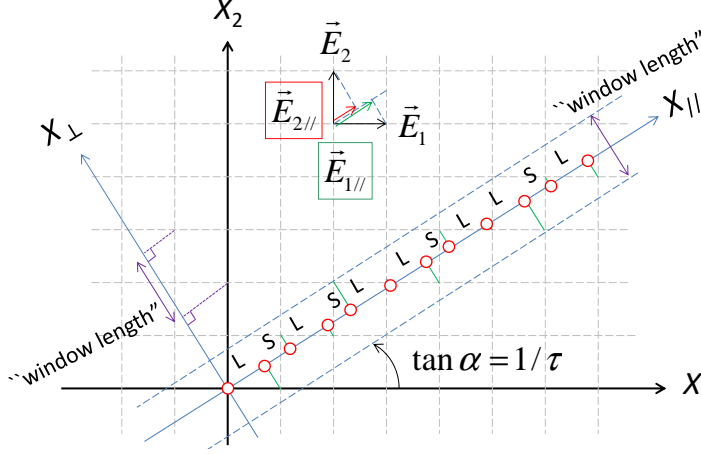


**Figure 1.6:** Construction of the 1 dimensional quasiperiodic arrangement from the 2 dimensional periodic square lattice.  $\vec{E}_{1\parallel}$  and  $\vec{E}_{2\parallel}$  are the basis vector of the 1 dimensional quasiperiodic lattice, respectively.

Each ratio corresponds to the approximant crystal: 1/1 approximant, 2/1 approximant, and so on. In the limit of  $N \rightarrow \infty$ , this ratio equals  $\tau$ . This periodic structure in the approximant crystal is also obtained by projection method. To show this, we set the angle  $\alpha$  such that  $\tan\alpha = 1/1$  for the 1/1 approximant (see Fig. 1.7). This choice of  $\alpha$  corresponds to the “phason strain”. Thus obtained periodic lattice shows periodic arrangement of SLSLSL  $\dots$ . This explains why the approximant is called “1/1 approximant”: the unit cell consists of SL, and the number ratio of L to S is 1/1.

When we set the window such that  $\tan\alpha = 1/2$ , another periodic lattice is obtained from the projection method (see Fig. 1.8). The unit cell of this lattice consists of LSL, and the number ratio of L to S is 2/1. Therefore, this periodic structure is called 2/1 approximant crystal.

The degree of the approximation is reflected in the lattice constant. For example, the lattice constant  $a_{1/1}$  of the 1/1 approximant is described as follows:

$$a_{1/1} = 1|L| + 1|S|, \quad (1.10)$$

$$|L| = \cos\theta \times \sqrt{2}a_{2D}, \quad (1.11)$$

$$|S| = \sin\theta \times \sqrt{2}a_{2D}. \quad (1.12)$$

Here,  $\theta$  is the angle between  $X_1$  and  $X_{\parallel}$ .  $|L|$  is the length of the longer portion L, and  $|S|$  is the length of the shorter portion S. The factor  $\sqrt{2}$

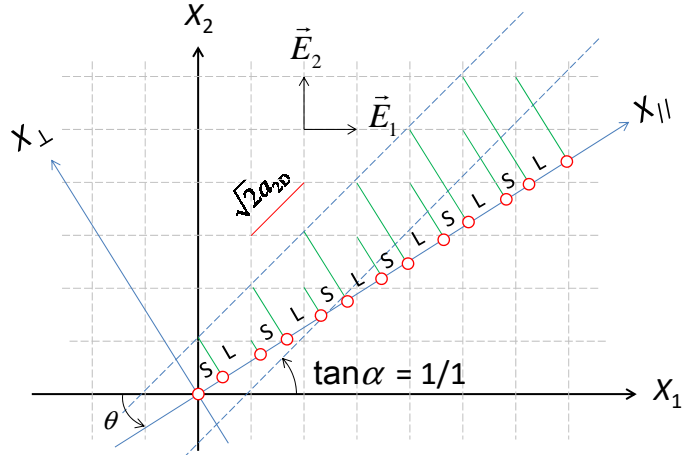


**Figure 1.7:** Construction of the periodic arrangement of 1/1 approximant crystal from the 2 dimensional periodic square lattice.

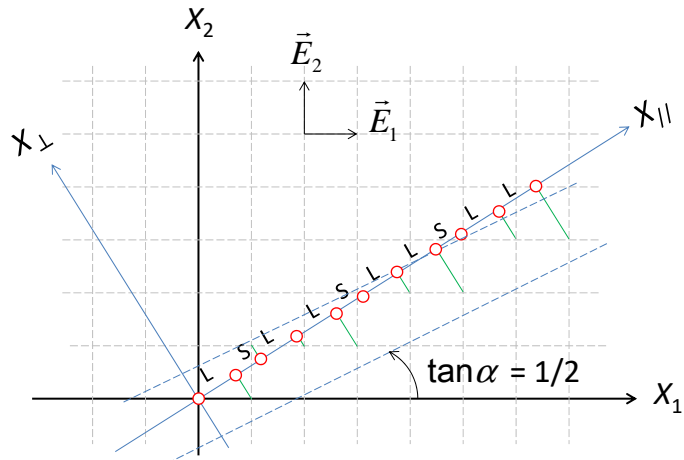


**Figure 1.8:** Construction of the periodic arrangement of 2/1 approximant crystal from the 2 dimensional periodic square lattice.

is needed to correct the length of the basis vector multiplied  $1/\sqrt{2}$  for the

projection. Since  $\tan\theta = 1/\tau$ ,  $\cos\theta$  and  $\sin\theta$  are given as follows:

$$\cos\theta = \frac{1}{\sqrt{1 + \tan^2\theta}} = \frac{\tau}{\sqrt{1 + \tau^2}} = \frac{\tau}{\sqrt{2 + \tau}}, \quad (1.13)$$

$$\sin\theta = \frac{\tan\theta}{\sqrt{1 + \tan^2\theta}} = \frac{1}{\sqrt{1 + \tau^2}} = \frac{1}{\sqrt{2 + \tau}}. \quad (1.14)$$

By substituting Eqs. 1.13 and 1.14 into Eq. 1.10, Eq. 1.10 is described as follows:

$$a_{1/1} = 1 \times \frac{\tau}{\sqrt{2 + \tau}} \sqrt{2}a_{2D} + 1 \times \frac{1}{\sqrt{2 + \tau}} \sqrt{2}a_{2D}. \quad (1.15)$$

For the  $A_N/A_{N-1}$  approximant crystal, the lattice constant  $a_{A_N/A_{N-1}}$  is given by

$$a_{A_N/A_{N-1}} = A_N \times \frac{\tau}{\sqrt{2 + \tau}} \sqrt{2}a_{2D} + A_{N-1} \times \frac{1}{\sqrt{2 + \tau}} \sqrt{2}a_{2D}. \quad (1.16)$$

Thus, the lattice constant increases as the degree of the approximation comes better, i.e.,  $N \rightarrow \infty$ , meaning that the lattice constant of the quasicrystal is infinite.

### 1.3 Heavy fermions

The electrons in metals may be classified into itinerant electrons and localized electrons. The itinerant electrons can jump onto the neighboring atoms. The wavefunction of the itinerant electrons expands over the crystal lattice. On the other hand, the localized electrons can not jump onto the neighboring atoms and remain on the same atom, and their wavefunctions are localized. Basically,  $4f$  electrons in rare earth elements are localized electrons. In heavy fermions such as Ce- and Yb-based materials, however,  $4f$  electrons can slightly move onto the neighboring atoms. When two electrons meet on the same  $4f$  orbital, there appears a large Coulomb repulsion between them. As a result,  $f$  electrons become difficult to move in the crystal, which gives the electrons the heavy mass. This is the reason why these electrons are called heavy electrons (heavy fermions). While a localized electron with spin of  $s = 1/2$  has the entropy of  $S = k_B \ln 2$  per electron, an itinerant electron system has the entropy of  $S = \gamma T$ . Here,  $k_B$  is the Boltzmann constant and  $\gamma$  is the electronic specific heat coefficient, which is proportional to the effective mass  $m^*$  of the electron. In the case of conventional metals such as Cu,  $m^*$  is of the same order as the free electron. For the system consisting of a mole of electrons, the entropy  $\gamma T$  at room temperature is smaller than the localized spin entropy,  $R \ln 2$ . Here,  $R$  is the gas constant. This feature is

schematically illustrated in Fig. 1.9: the itinerant-electron entropy denoted by the dotted line is smaller than the localized-electron entropy denoted by the broken line.

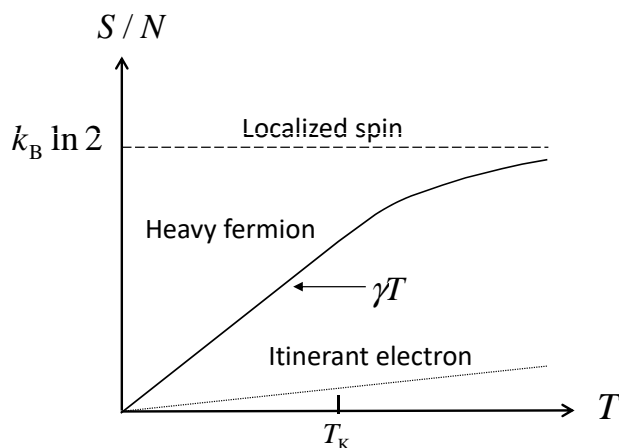


**Figure 1.9:** Temperature dependence of the entropy  $S$ .  $N$  is numbers of spins.

In the case of heavy fermion systems, the  $4f$  electron behaves like an itinerant electron in the low temperature region and like a localized electron in the high temperature region. The crossover temperature between the itinerant and localized characters is called Kondo temperature  $T_K$ , which is a few Kelvin for the conventional heavy fermion systems. As a result, the entropy shows a large slope as shown in Fig. 1.9. This large slope means that  $\gamma$  and hence  $m^*$  is much enhanced, and such the enhanced specific heat  $C$  is often observed experimentally.  $C$  and  $S$  are related by the following equation,

$$S = \int \frac{C}{T} dT. \quad (1.17)$$

Figure 1.10 shows the temperature dependence of  $C/T$  of the heavy fermion materials. As the temperature is decreased,  $C/T$  increases and saturates at a huge value. This behavior at  $T \ll T_K$  means that the heavy fermions become the Fermi liquid. Note that the Fermi liquid behavior is described as follows:  $C/T \sim \text{constant}$ ,  $\chi \sim \text{constant}$ ,  $\rho \propto T^2$ . Here,  $\chi$  and  $\rho$  are the magnetic susceptibility and the electrical resistivity, respectively. Some of the heavy fermion systems (for example, CeCu<sub>6</sub> [7]) remain to be Fermi liquid down to zero temperature. Some of them (for example, CeB<sub>6</sub> [8]) undergo a magnetically ordered state and/or a superconducting state. The

difference of the ground state occurs as a result of the competition between the RKKY interaction and the Kondo effect, i.e., the exchange interaction between the itinerant electrons and the localized spins.

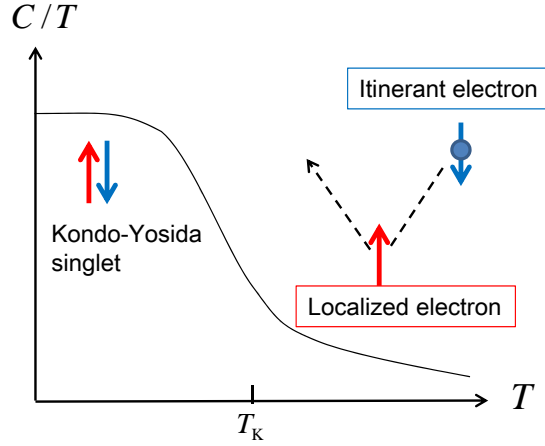


**Figure 1.10:** Temperature dependence of the specific heat divided by temperature  $C/T$ . At  $T \gg T_K$ , the itinerant electrons are scattered by the localized spin. While at  $T \ll T_K$ , the itinerant electrons are by the localized electrons, forming the ground state called the Kondo-Yosida singlet state.

### 1.3.1 Quantum critical phenomena

There are a number of materials which undergo a ferromagnetically or an antiferromagnetically ordered state at low temperature. We denote the transition temperature as  $T_m$ . When the magnetic materials are pressurized,  $T_m$  may decrease with increasing pressure. In such case, the transition temperature  $T_m$  can be zero, where the quantum phase transition occurs (see Fig. 1.11). If the transition is of the second order type, the transition point is called the quantum critical point (QCP). On the other hand, if the pressure is increased at  $T = 0$ , then this magnetic material undergoes a phase transition from the magnetic state to the paramagnetic state at the QCP.

In the quantum critical region as schematically shown by the purple shaded region in Fig. 1.11, unusual physical properties are observed. Here, “unusual” means that the temperature dependence is different from that of the Fermi liquid. This non-Fermi liquid is often understood by the so-called SCR theory [9]. Recently, some materials in which the physical properties are not described by the SCR theory have been observed. In this thesis, we

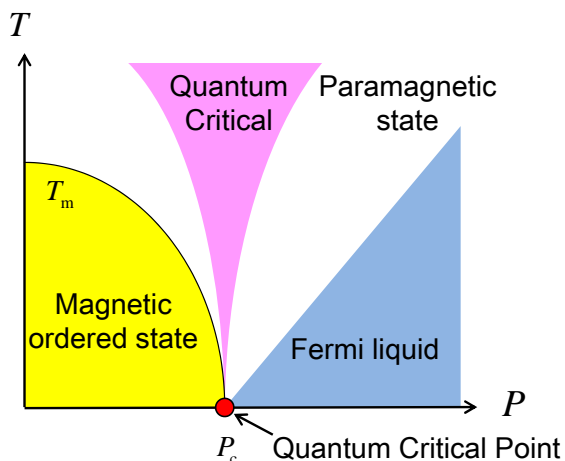


**Figure 1.11:** Schematic  $P$ - $T$  phase diagram.  $T_m$  and  $P_c$  are the magnetic transition temperature and the critical pressure, respectively.

show that the Au-Al-Yb quasicrystal and the approximant are an example of such the novel materials.

## 1.4 Au-Al-Yb quasicrystal and approximant

### 1.4.1 Structure model

The geometric structure of the Au-Al-Yb quasicrystal and the approximant can be understood using the structure model of the Cd- $R$  approximant ( $R$  = rare-earth element) [10,11]. The icosahedrons are arranged quasiperiodically with a fivefold diffraction symmetry in the quasicrystal (Fig. 1.12 (a)), while in the 1/1 approximant, they are arranged periodically to form a body-centered cubic (bcc) structure (space group:  $Im\bar{3}$ ) (Fig. 1.12 (b)). This bcc structure of the icosahedrons may be more clearly seen in Fig. 1.12 (b); each icosahedron has edge lengths of 5.45 and 5.49 Å, and the interatomic distance between the neighboring icosahedrons is 5.33 and 5.69 Å [1]. These distances are so large that there is no direct overlap between the  $4f$  electron wavefunctions derived from the Yb ions. Figure 1.13 shows a structure model of the Au-Al-Yb 1/1 approximant determined by the Rietveld method. The square frame indicates the unit cell with a size of the lattice parameter  $a = 14.500$  Å. The Tsai-type cluster consists of concentric arrangement of triple shells (see Fig. 1.4); at the center of the first shell, there is a polyhedron labeled M7 (see Fig. 1.13 (a)). Here, the green sphere denotes

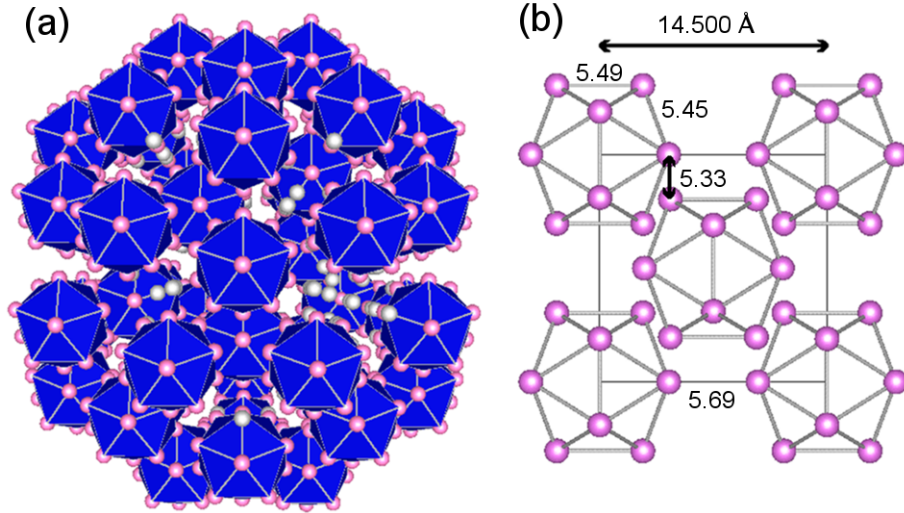


**Figure 1.12:** Geometric structure of the Tsai-type quasicrystal and its approximant crystal [1,2]. (a) Aperiodic array of icosahedrons (denoted by blue polyhedron) in the quasicrystal. Rose-pink and gray spheres denote Yb ions located on the vertices of an icosahedron and in an acute rhombohedron (see Fig. 1.14 (b)), respectively. (b) Network of Yb ions in the Au-Al-Yb 1/1 approximant. This constructs the body-centered cubic structure. The number denotes the length in the unit of Å.

the site alternatively occupied by Au and Al. This polyhedron consists of four atoms in total (abbreviated as 4 Au/Al atoms in this thesis) and is represented by a complicated polyhedron reflecting an average of variously oriented tetrahedrons. Figure 1.13 (b) shows the first and second shells, in which one may find a pentagon beneath the rose-pink sphere (representing Yb) consisting of three green spheres (M2) and two yellow spheres (M4). Note that the rose-pink sphere site is occupied by Yb, and the yellow one is preferably occupied by Au. Figure 1.13 (c) shows the second and third shells, in which one may find another pentagon (consisting of four yellow spheres (M1) and one green sphere (M6)) around Yb. As seen in Fig. 1.13 (d), five yellow spheres (M1 and M3) form a pentagon around the blue sphere (M5); here, the blue sphere indicates the site almost occupied by Al.

The three pentagons together with the blue (M5) and green (M7) spheres are arranged as shown in Fig. 1.14 (a). This figure may best visualize the local environment of the Yb ion. In this structure model of the approximant, the Yb ion site is uniquely determined and referred to as the A-site hereafter.

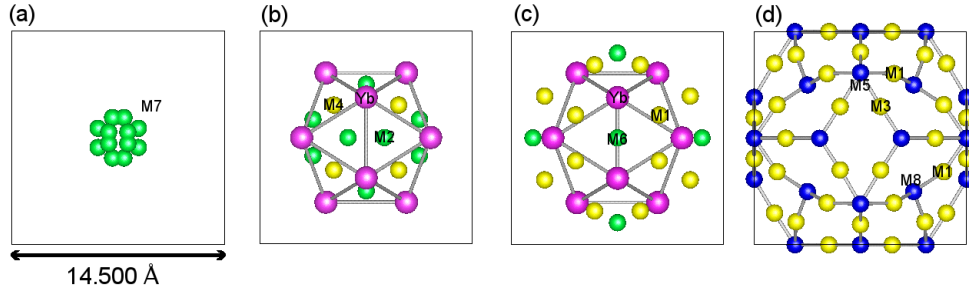


**Figure 1.13:** Structure model of Tsai-type cluster in Au-Al-Yb 1/1 approximant [12]. Rose-pink: Yb, blue: Al, yellow: Au, green: Au/Al. The square frame of each panel indicates the unit cell size of the lattice parameter  $a = 14.500 \text{ \AA}$ . (a) Local structure at the center of the cluster. The tetrahedron is oriented in a disordered fashion, and the average of the various orientations leads to the complicated polyhedron structure. (b) First and second shells of the cluster. (c) Second and third shells of the cluster. (d) Triacotahedron decorated by Au and Al atoms.

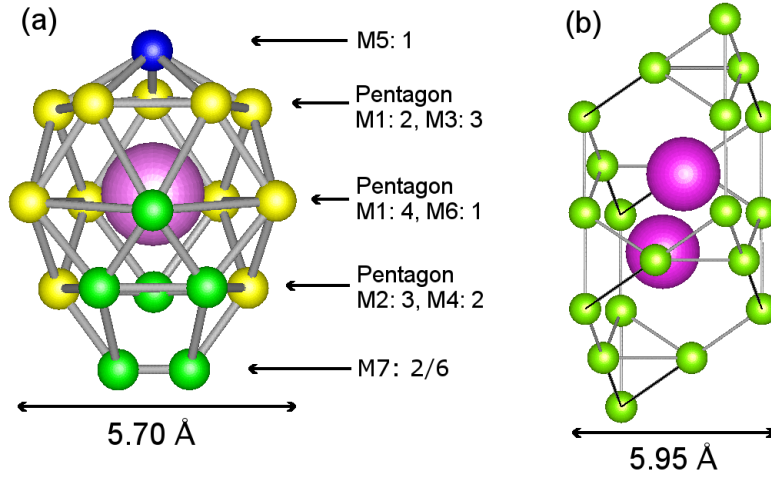
By analogy with Cd-*R* quasicrystals [11], on the other hand, there are two Yb sites in the Au-Al-Yb quasicrystal: one is the A-site and the other is a specific site (referred to as the B-site hereafter) embedded in the so-called acute rhombohedron (see Fig. 1.14 (b)). Each acute rhombohedron includes two B-sites with a distance of about  $3.4 \text{ \AA}$ , which is too large to give rise to a direct overlap between the  $4f$  wavefunctions. Note that the population ratio of the A- and B-sites is approximately  $7 : 3$ .

According to a nuclear magnetic resonance measurement for the Au-Al-Yb quasicrystal and the approximant (see below), nuclear magnetization recoveries after saturation pulses were fit using a theoretical function with a single component of  $T_1$  ( $T_1$  is a nuclear spin-lattice relaxation time) for both the quasicrystal and the approximant. This suggests that the electronic state is rather homogeneous even in the quasicrystal.

## 1.4.2 Physical properties

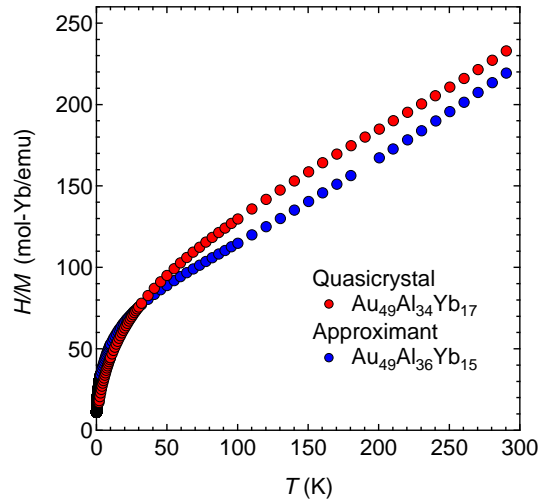
### Dc magnetization

Figure 1.15 shows the temperature dependence of the inverse magnetic susceptibility of the Au-Al-Yb quasicrystal and the approximant. Above  $100 \text{ K}$ , both the quasicrystal and the approximant show the Curie-Weiss like feature. The effective moments of the quasicrystal and the approximant are  $3.91\mu_B$  and  $3.96\mu_B$ , respectively. These values are smaller than that of



**Figure 1.14:** Geometric arrangement of Yb ions in the quasicrystal and the approximant [12]. (a) Coordination polyhedron of Yb. (b) Acute rhombohedron of Yb in the Cd-Yb quasicrystal, in which green spheres indicate Cd. This type of Yb site is missing in 1/1 approximants.

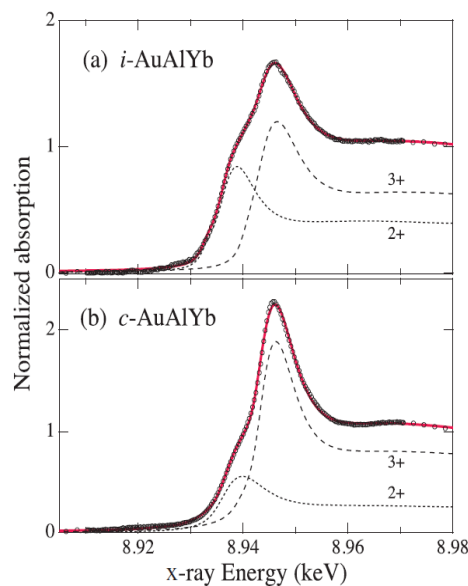
the free  $\text{Yb}^{3+}$  ion,  $4.54\mu_B$ , and larger than that of the free  $\text{Yb}^{2+}$  ion, 0. This suggests that the Yb-ion of the quasicrystal and the approximant is in between  $\text{Yb}^{3+}$  and  $\text{Yb}^{2+}$ .



**Figure 1.15:** Temperature dependence of the inverse magnetic susceptibility of the Au-Al-Yb quasicrystal and approximant [2].

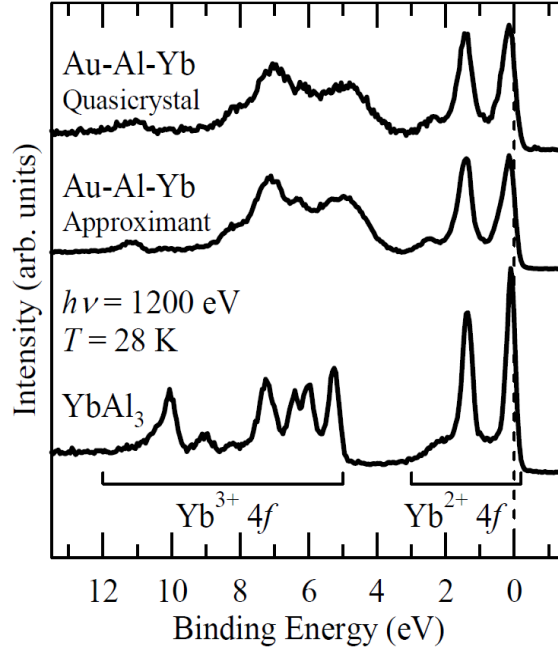
## X-ray absorption near-edge structure experiments and photo emission spectroscopy

Figure 1.16 shows the normalized X-ray absorption near-edge structure (XANES) spectra of the Au-Al-Yb quasicrystal (a) and the approximant (b), where the absorption edge spectrum obviously exhibits a double peak [13]. The lower energy peak around 8.939 keV corresponds to the divalent component, while the higher one around 8.946 keV corresponds to the trivalent one. These results indicate that an intermediate valence state is realized in the Au-Al-Yb quasicrystal and the approximant. Figure 1.17 shows the



**Figure 1.16:** Normalized Yb  $L_3$  XANES spectra of Au-Al-Yb quasicrystal (a) and approximant (b) at room temperature (open circles) [13]. Each spectrum is fitted by the sum (solid red line) of divalent (dotted line) and trivalent (dashed line) components.

photoemission spectra of the Au-Al-Yb quasicrystal, the approximant, and  $\text{YbAl}_3$ , which is a typical valence fluctuation system [14]. In  $\text{YbAl}_3$ , the two sharp peaks observed between  $E_F$  and 2 eV are derived from the  $\text{Yb}^{2+}$ . The other sharp peaks observed between 5 and 12 eV are derived from the  $\text{Yb}^{3+}$ . It is important to note that the  $\text{Yb}^{2+}$  peak crosses  $E_F$ . This means that the valence fluctuates in time and space. For the Au-Al-Yb quasicrystal and the approximant, both of the peaks from the  $\text{Yb}^{2+}$  and the  $\text{Yb}^{3+}$  are observed. Note again that the  $\text{Yb}^{2+}$  peak crosses  $E_F$ . Therefore, the Yb ions of the quasicrystal and the approximant are found to fluctuate between  $\text{Yb}^{3+}$  and  $\text{Yb}^{2+}$ .



**Figure 1.17:** Photoemission spectra of the Au-Al-Yb quasicrystal, the approximant, and  $\text{YbAl}_3$  at 28 K [14].

### Specific heat

Figure 1.18 shows the temperature dependence of the magnetic part ( $C_M/T$ ) of the specific heat coefficient of the Au-Al-Yb quasicrystal (a) and the approximant (b). Here,  $C_M$  was obtained by subtracting the nuclear and phonon contributions from the measured specific heat. For the quasicrystal, logarithmic divergence at zero field is observed in the temperature dependence,  $C_M/T \propto -\ln T$ . By applying magnetic fields, the divergence is suppressed, but the saturated value is still very large;  $C_M/T \sim 200 \text{ mJ/K}^2\text{mol}$  at  $H = 50 \text{ kOe}$ . By contrast, the approximant shows no divergence. Again, the saturated value is very large,  $\sim 700 \text{ mJ/K}^2\text{mol}$ , compared with conventional crystals. The application of magnetic fields suppresses the increase in  $C_M/T$ .

### Ac magnetic susceptibility

Figures 1.19 (a) and (b) show the temperature dependence of the magnetic susceptibility of the Au-Al-Yb quasicrystal and the approximant, respectively. The magnetic susceptibility of the quasicrystal at  $H = 0$  shows a divergent behavior as  $T \rightarrow 0$ . The inverse magnetic susceptibility shows a good

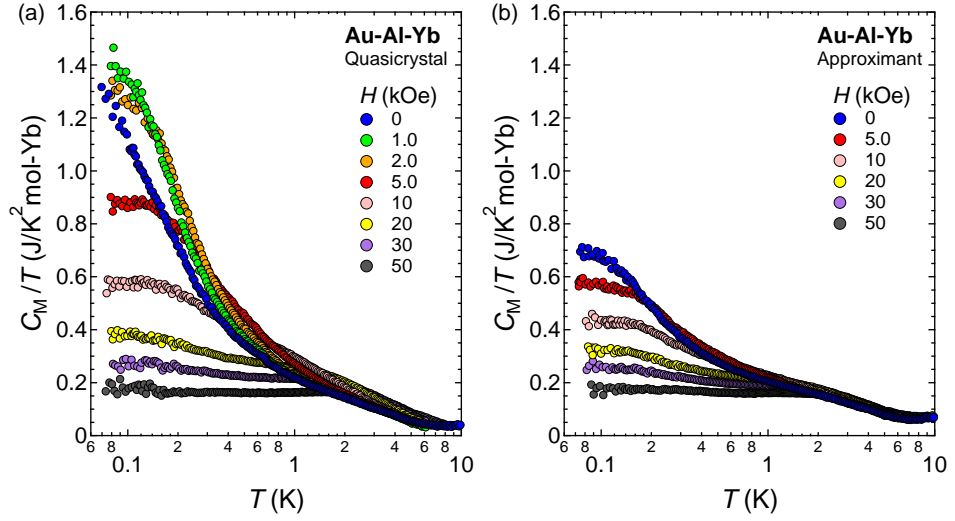


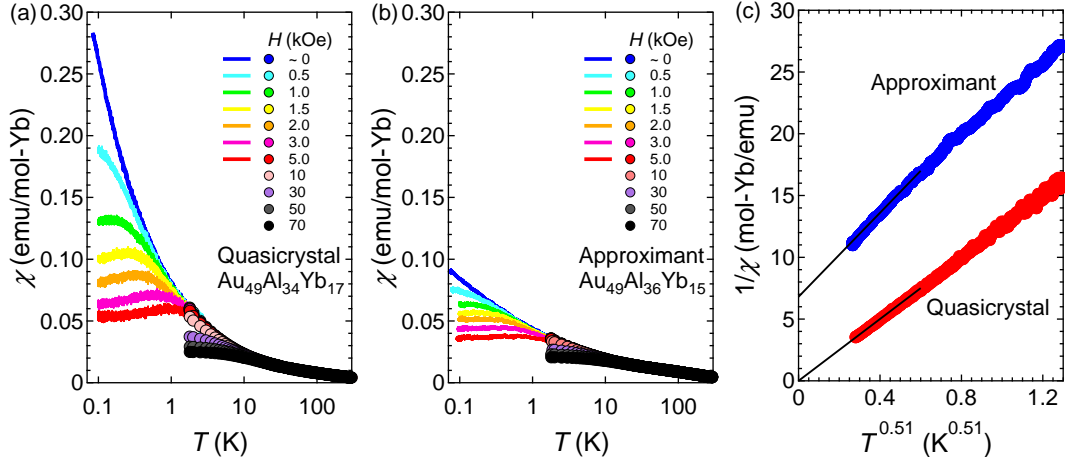
**Figure 1.18:** Temperature dependence of the magnetic specific heat  $C_M/T$  of the quasicrystal (a) and approximant (b) under magnetic field [2].

linearity as a function of  $T^{0.51}$  (see Fig. 1.19 (c)). Note that the straight line goes through the origin. This confirms that the magnetic susceptibility diverges toward zero temperature. This quantum criticality is characterized by a critical index  $n \simeq 0.51$ . In contrast, although the magnetic susceptibility of the approximant at  $H = 0$  increases with decreasing temperature, the magnetic susceptibility does not diverge, as evidenced from the presence of the constant term in the equation of  $\chi^{-1} \propto T^n + \text{constant}$  ( $n \sim 0.5$ ).

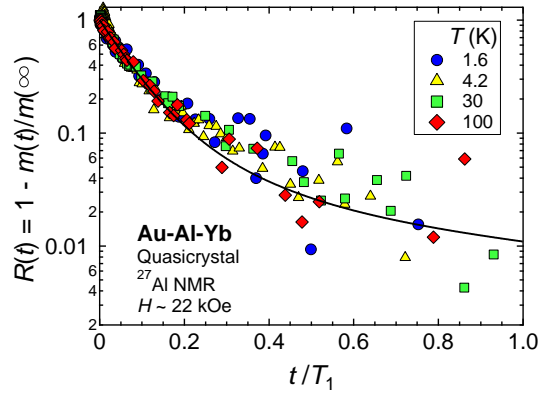
### Nuclear magnetization recoveries after saturation pulses

Figure 1.20 shows the recovery of the nuclear magnetization after a saturation pulse in the Au-Al-Yb quasicrystal. Nuclear magnetization recoveries after saturation pulses, which were taken from the  $1/T_1T$  measurements, were fit by the theoretical function with a single component of  $T_1$  in the whole temperature range measured. This suggests that the electronic state in the Au-Al-Yb quasicrystal is homogeneous as mentioned above.

Figure 1.21 shows the nuclear spin-lattice relaxation rate divided by temperature,  $1/T_1T$ , deduced from  $^{27}\text{Al}$  nuclear magnetic resonance (NMR) measurements on the quasicrystal. Whereas the uniform susceptibility  $\chi(T)$  probes magnetic fluctuations at  $\vec{q} = 0$  (where  $\vec{q}$  is the wave vector of an applied magnetic field),  $1/T_1T$  observes the  $\vec{q}$ -averaged fluctuations. The scaling observed here,  $1/T_1T \propto \chi$ , together with a negative Weiss temperature suggest that  $\chi(q)$  is independent of  $|\vec{q}|$ , meaning that the magnetic



**Figure 1.19:** Temperature dependence of the magnetic susceptibility of the Au-Al-Yb quasicrystal (a) and approximant (b) [2]. (c) The inverse magnetic susceptibility versus  $T^{0.51}$  of the quasicrystal (red circles) and approximant (blue circles) at  $H = 0$  and at ambient pressure.



**Figure 1.20:** The recovery of the nuclear magnetization after a saturation pulse of the Au-Al-Yb quasicrystal [2]. The data are well fit by a theoretical curve with a single component  $T_1$  denoted by the solid line.

fluctuation associated with the quantum criticality possesses a local nature in the real space.

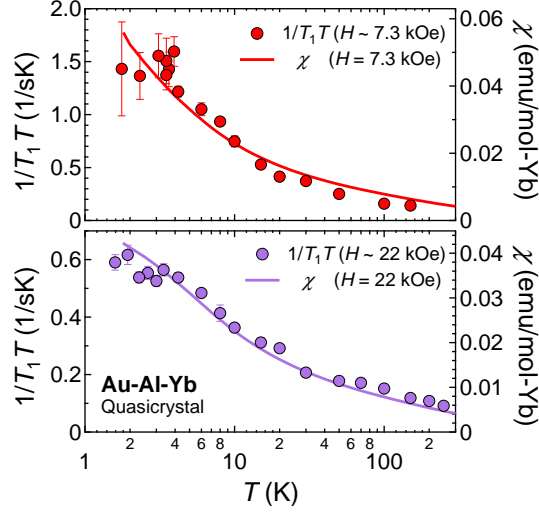


**Figure 1.21:** Temperature dependence of the nuclear spin-lattice relaxation rate divided by temperature  $1/T_1T$  of  $^{27}\text{Al}$  NMR (left axis) and the uniform magnetic susceptibility  $\chi$  (right axis) [2].

### Electrical resistivity

Figure 1.22 (a) shows the temperature dependence of the electrical resistivity of the Au-Al-Yb quasicrystal and the approximant. The residual resistivity is 199 and 161  $\mu\Omega\text{cm}$  for the quasicrystal and the approximant, respectively. Figures 1.22 (b) and (c) show the temperature dependent part  $\Delta\rho = \rho(T) - \rho(0)$  as a function of  $T$  and  $T^2$  below 25 K, respectively. The quasicrystal shows the non-Fermi liquid behavior  $\Delta\rho \propto T$ , while the approximant indicates the Fermi liquid feature  $\Delta\rho \propto T^2$  as in a conventional metal.

### Origin of the unconventional quantum criticality of the Au-Al-Yb quasicrystal

As shown previous sections, the uniform susceptibility  $\chi$  of the quasicrystal shows the power law divergence with the critical index -0.51 (see table 1.1). The nuclear spin-lattice relaxation rate divided by temperature  $1/T_1T$  is proportional to  $\chi$ . The specific heat divided by temperature  $C/T$  shows the logarithmic divergence. The low-temperature resistivity  $\Delta\rho = \rho(T) - \rho(0)$  is proportional to  $T$ . Theoretically, the local criticality model [15] and the Kondo disorder model [16] can not explain these results. In contrast, the critical valence fluctuation model [17] may explain these experimental results. This is discussed later in this thesis.

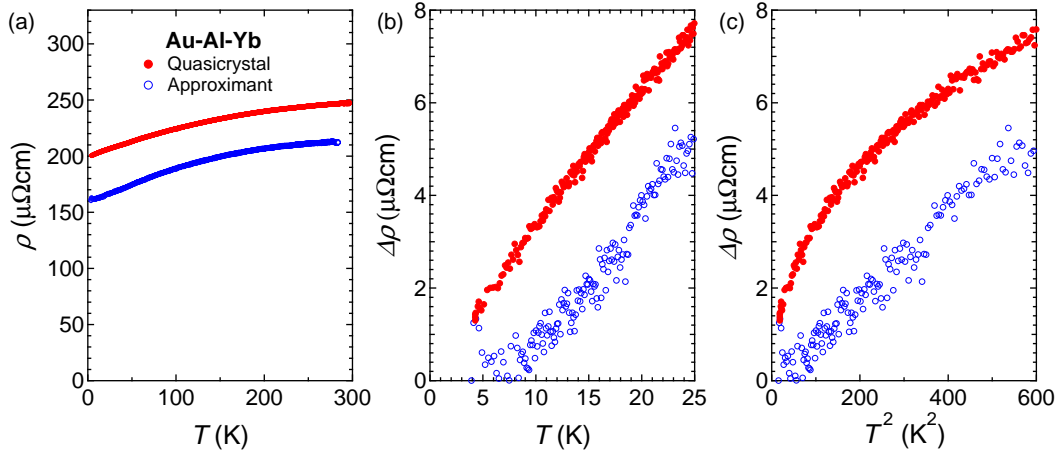


**Figure 1.22:** (a) Temperature dependence of the electrical resistivity of the Au-Al-Yb quasicrystal and the approximant [2]. (b) and (c) show the temperature dependent part  $\Delta\rho = \rho(T) - \rho(0)$  as a function of  $T$  and  $T^2$ , respectively.

### Pressure effect on the quantum criticality of the Au-Al-Yb quasicrystal and its approximant

As mentioned above, the quasicrystal is located at the QCP, while the approximant is away from the QCP. In heavy fermion crystals, the application of external pressure changes the distance from the QCP (see Fig. 1.23). For the present systems (i.e., the Au-Al-Yb quasicrystal and its approximant), the pressure effect is not reported yet. To reveal this is one of the purposes in this thesis.

## 1.5 Purposes of this thesis

As mentioned above, the Au-Al-Yb quasicrystal and the approximant show the different physical properties at low temperatures (see section 1.4.2). We expect that this difference is related to the quasiperiodicity in the quasicrystal. One of the purposes of this thesis is to reveal the physical properties unique to the quasicrystal by studying the pressure effect on the Au-Al-Yb quasicrystal and the approximant. The second purpose is to reveal the origin of the quantum criticality of the Au-Al-Yb quasicrystal.

	Au-Al-Yb Quasicrystal	$\beta$ -YbAlB <sub>4</sub>	YbRh <sub>2</sub> Si <sub>2</sub>	Valence Criticality	Local Criticality	Kondo disorder Griffiths phase
$1/\chi$	$T^{0.51}$	$T^{0.5}$	$T^{0.6}$	$T^{0.5-0.7}$	$T^\alpha + \text{const.}$ ( $\alpha < 1$ )	$T^{\lambda-1}$ ( $0 < \lambda < 1$ )
$1/T_1T$	$\propto \chi$	-	$T^{-0.5}$	$\propto \chi$	$T^{-1}$	-
$C/T$	$-\ln T$	$-\ln T$	$-\ln T$	$-\ln T$	-	$\propto \chi$
$\Delta\rho$	$T$	$T^{1.5} \rightarrow T$ (low- $T$ )	$T$	$T$	-	$-T$

**Table 1.1:** Exponents of some Yb-based materials together with those predicted by theories.  $1/\chi$ ,  $1/T_1T$ ,  $C/T$  are the inverse of the uniform magnetic susceptibility, the nuclear spin-lattice relaxation rate divided by temperature, and the specific heat divided by temperature, respectively.  $\Delta\rho$  ( $= \rho(T) - \rho(0)$ ) is the low-temperature resistivity.

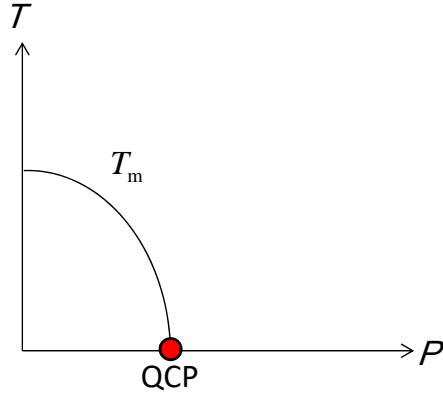


**Figure 1.23:** Schematic  $P$ - $T$  phase diagram. The red point indicates the QCP.  $T_m$  indicates the magnetic transition temperature.

## Chapter 2

# Pressure Effect on Quantum Criticality of the Au-Al-Yb Quasicrystal

### 2.1 Introduction

As shown in the previous chapter, the quasicrystal shows the unconventional quantum criticality at ambient pressure, i.e., without tuning. In this chapter, we investigate the pressure effect on the quantum criticality of the quasicrystal. In contrast to heavy fermions, in which the quantum criticality is tuned by external parameters such as pressure, we find that the quantum critical behavior of the quasicrystal is robust against the application of hydrostatic pressure.

### 2.2 Experimental Method

A quasicrystal with the nominal composition,  $\text{Au}_{49}\text{Al}_{34}\text{Yb}_{17}$ , was prepared by arc-melting the starting materials of 4N (99.99% pure)-Au, 5N-Al, and 3N-Yb. The ac magnetic susceptibility was measured by conventional mutual inductance method. Figure 2.1 shows the schematic illustration of the ac magnetic susceptibility measurement under pressure. A modulation field with a frequency of 100.3 Hz and an amplitude of 0.1 Oe was superimposed on a dc magnetic field supplied by a superconducting magnet. For the calibration of the ac magnetic susceptibility, we measured the dc magnetization using MPMS (Quantum Design) at pressures up to 1 GPa, above which we extrapolated the dc magnetization data. The electrical resistivity was measured by a conventional dc 4-probe method in a temperature range of 2 K and room temperature. Hydrostatic pressure was generated using a

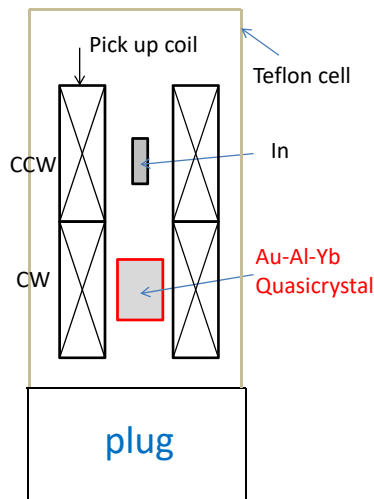


**Figure 2.1:** Schematic illustration of the ac magnetic susceptibility measurement under pressure. CW and CCW denote the coil wound clockwise and counter clockwise, respectively.

BeCu piston cylinder cell and a NiCrAl-BeCu piston cylinder cell for measurement of dc magnetization and ac susceptibility, respectively. We used Daphne oil 7373 as a pressure-transmitting medium. The pressure at low temperature was determined from the superconducting transition temperature of indium [18] that was put into the pressure cell together with the sample.

## 2.3 Results and Discussion

### 2.3.1 Dc magnetization of the Au-Al-Yb quasicrystal under hydrostatic pressure

Figure 2.2 shows the magnetization curves of the Au-Al-Yb quasicrystal at  $T = 2$  K under pressure. The magnetization  $M$  at a fixed field  $H$  monotonically increases with pressure.  $M$  shows good linearity as a function of  $H$  up to 3 kOe. This means that  $M/H$  equals  $\chi(= dM/dH)$ , which helps us to calibrate the ac magnetic susceptibility (see below). Figure 2.3 shows the pressure dependence of  $M/H$  of the quasicrystal at 2 K.  $M/H$  monotonically increases with pressure. To calibrate the ac magnetic susceptibility,  $M/H$

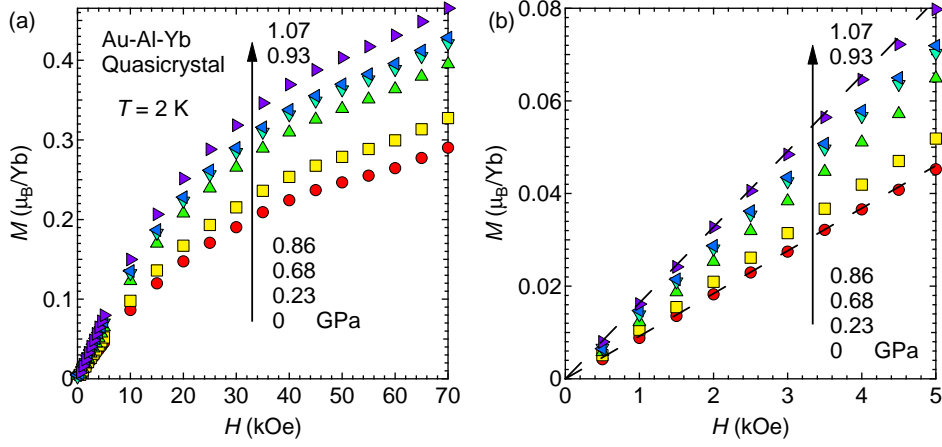
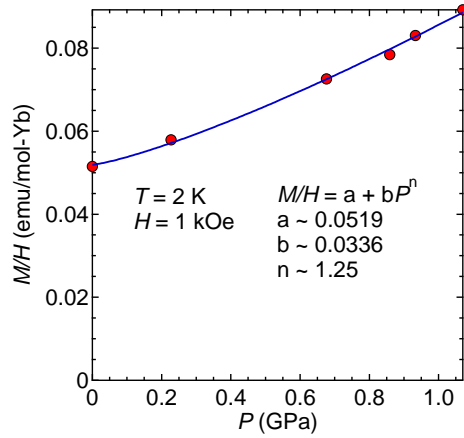


**Figure 2.2:** (a) Magnetic field dependence of the magnetization of the Au-Al-Yb quasicrystal under pressure. (b) Magnetization below 5 kOe. The dashed line is a guide to the eyes.

was fitted to the following equation,

$$\frac{M}{H} = a + bP^n. \quad (2.1)$$

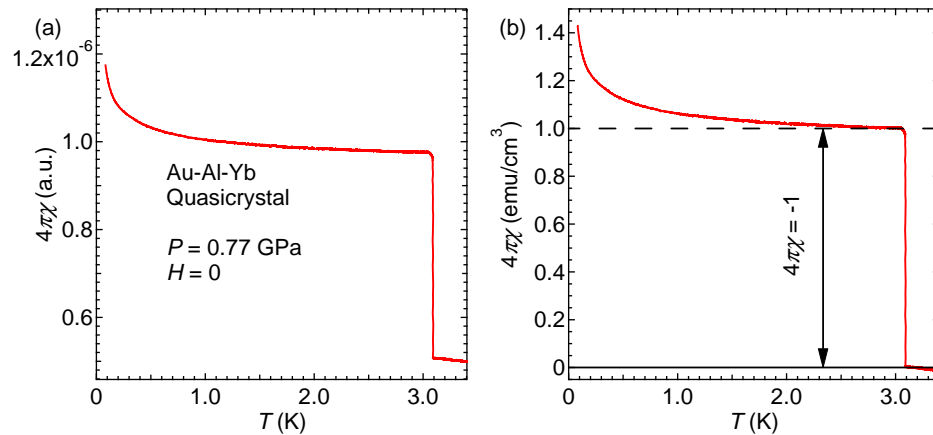
As shown in Fig. 2.3, we obtain the following values:  $a = 0.0519 \pm 0.0002$ ,  $b = 0.0336 \pm 0.0003$ , and  $n = 1.25 \pm 0.03$ .



**Figure 2.3:** Pressure dependence of the magnetic susceptibility of the quasicrystal at 2 K. The blue curve denotes the result of fitting.

### 2.3.2 Calibration method of ac magnetic susceptibility under pressure

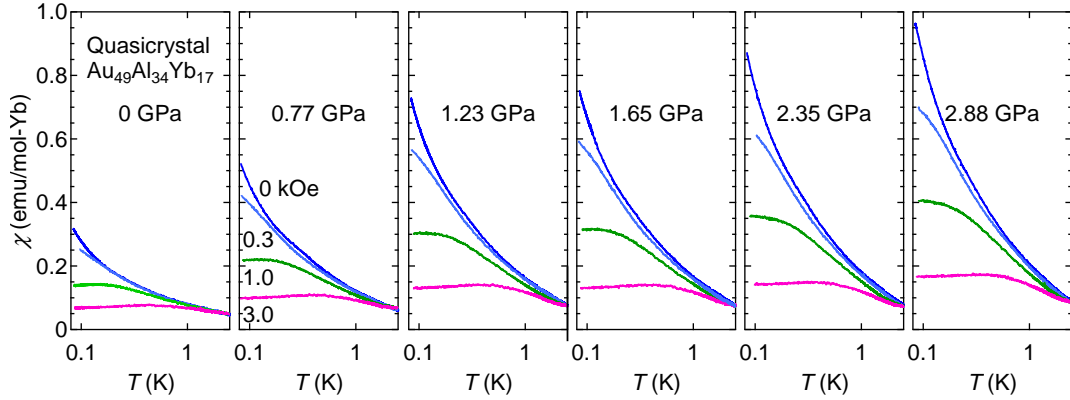
We need to calibrate the ac magnetic susceptibility under pressure. To do so for the ambient pressure measurement, we measured the dc magnetization in the same temperature interval as the ac susceptibility. However, this method is not applicable to the high pressure experiments, because it was difficult to measure the temperature dependence of the dc magnetization under pressure exceeding about 1.5 GPa. To avoid this difficulty, we measured the superconducting transition of indium to determine the sensitivity of the pick up coil used here, assuming that the jump in the superconducting diamagnetism of indium does not depend on pressure, with  $4\pi\chi = -1$  emu/cm<sup>3</sup> (see Fig. 2.4). Then, using the result of Fig. 2.3, we determined the zero of ac magnetic susceptibility.



**Figure 2.4:** Temperature dependence of the magnetic susceptibility at 0.77 GPa. The vertical axis is given in an arbitrary unit (a) and in a calibrated unit (b).

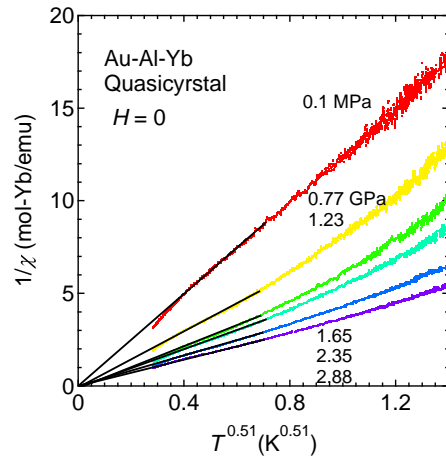
### 2.3.3 Magnetic susceptibility of the Au-Al-Yb quasicrystal under hydrostatic pressure

Figure 2.5 shows the temperature dependence of the magnetic susceptibility of the Au-Al-Yb quasicrystal at dc magnetic fields and at hydrostatic pressures. The low-temperature susceptibility for  $H = 0$  increases with pressure, whereas the application of the dc magnetic field suppresses this increase. Figure 2.6 shows the inverse magnetic susceptibility  $1/\chi$  of the quasicrystal as a function of  $T^{0.51}$  at  $H = 0$  under pressure. The  $1/\chi$  vs  $T^{0.51}$  curve shows the good linearity between  $80 \leq T \leq 800$  mK, indicating



**Figure 2.5:** Temperature dependence of the magnetic susceptibility of the Au-Al-Yb quasicrystal in a temperature range of  $0.08 \leq T \leq 2$  K at pressures indicated in the figure. Applied dc magnetic fields are denoted in the figure of  $P = 0.77$  GPa.

that the divergent behavior survives under pressure, with the novel critical exponent unchanged.



**Figure 2.6:** Inverse magnetic susceptibility vs  $T^{0.51}$  of the Au-Al-Yb quasicrystal at  $H = 0$  under pressure ranging from ambient pressure to 2.88 GPa. The straight lines are linear extrapolations to  $T = 0$ .

### 2.3.4 Electrical resistivity of the Au-Al-Yb quasicrystal under hydrostatic pressure

Figure 2.7 shows the temperature dependence of the electrical resistivity under hydrostatic pressure. External pressure increases the magnitude of the electrical resistivity. Up to the highest pressure measured in the present study, no experimental evidence for a phase transition was found.

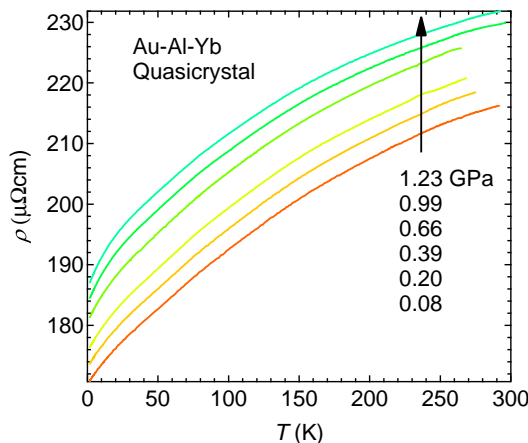


**Figure 2.7:** Temperature dependence of the electrical resistivity of the Au-Al-Yb quasicrystal in a temperature range of  $2 \leq T \leq 300$  K at pressure  $P = 0.08, 0.20, 0.39, 0.66, 0.99,$  and  $1.23$  GPa.

### 2.3.5 Origin of the robustness of the pressure effect

Let us discuss a possible origin of the robustness of the unconventional quantum criticality of the Au-Al-Yb quasicrystal. The robustness may be related to the quasiperiodicity because it was not observed in the approximant crystal as mentioned in the next chapter. However, another possibility (for example, chemical disorder, cluster structure, etc.) remains to be a possible origin. This will be discussed in the next chapter.

## 2.4 Summary

We measured the magnetic susceptibility of the Au-Al-Yb quasicrystal under hydrostatic pressure. The magnetic susceptibility at low temperature increases with pressure with no indication of the magnetic ordering. We have found that the quantum criticality of the quasicrystal is robust against

the application of the pressure up to 2.88 GPa (the highest pressure of the present measurement).



## Chapter 3

# Pressure-Driven Quantum Criticality in the Au-Al-Yb Approximant

### 3.1 Introduction

In the previous chapter, the unconventional quantum criticality of the quasicrystal was found to be robust against the application of the hydrostatic pressure. In this chapter, we study the magnetic properties of the Au-Al-Yb approximant under hydrostatic pressure. We find that the magnetic susceptibility of the approximant strongly increases with pressure and diverges toward  $T \rightarrow 0$  at  $P_c \sim 2$  GPa. This means that there is a quantum critical point (QCP) at  $P_c$ . At high pressures exceeding  $P_c$ , the approximant undergoes a spin-glass like short-range ordering at  $T_g \sim 100$  mK. These results indicate that the pressure effect on the approximant remarkably differs from that of the quasicrystal. This leads us to suggest that the robustness of the quantum criticality in the quasicrystal against hydrostatic pressure is related to the presence of the quasiperiodicity.

### 3.2 Experimental Method

The 1/1 approximant crystal with the nominal composition,  $\text{Au}_{49}\text{Al}_{36}\text{Yb}_{15}$ , was prepared by arc-melting the starting materials of 4N (99.99% pure)-Au, 5N-Al, and 3N-Yb, and subsequently annealing the obtained alloy ingot in an evacuated quartz ampoule at 750 °C for 116 h. The electrical resistivity was measured by the same method as done for the quasicrystal. The ac magnetic susceptibility was measured by the same method as done for the quasicrystal (see section 2.2). Figure 3.1 shows the schematic illustration

of the ac magnetic susceptibility measurement under pressure. To calibrate the sensitivity of the pick up coil carefully, we put the indium on the same side as the Au-Al-Yb approximant and measured the dc magnetization  $M$  using MPMS (Quantum Design) at pressures of up to 1.2 GPa, above which we extrapolated the dc magnetization data. A modulation field (with the frequency in the range of 10.03 to 3003 Hz and the amplitude of 0.1 Oe) for the ac susceptibility measurement was superimposed on a dc magnetic field  $H$  supplied by a superconducting magnet. We used the same piston cylinder cell and the pressure-transmitting medium as for the quasicrystal measurement. The pressure at low temperature was also determined in the same way as for the quasicrystal.

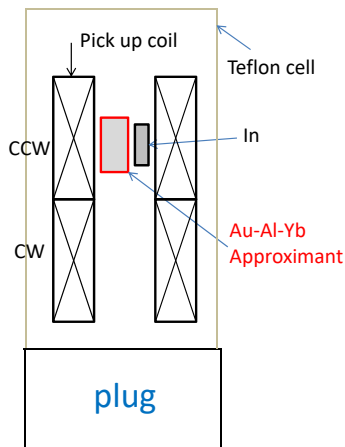


**Figure 3.1:** Schematic illustration of the ac magnetic susceptibility measurement under pressure. CW and CCW denote the coil wound clockwise and counter clockwise, respectively.

### 3.3 Results and Discussion

#### 3.3.1 Electrical resistivity of the Au-Al-Yb approximant under hydrostatic pressure

Figure 3.2 shows the temperature dependence of the electrical resistivity under hydrostatic pressure. Similar to the quasicrystal, external pressure increases the magnitude of the electrical resistivity. At the highest pressure (2.43 GPa), we note that there is a bend-like anomaly. This origin remain to be clarified in the future.

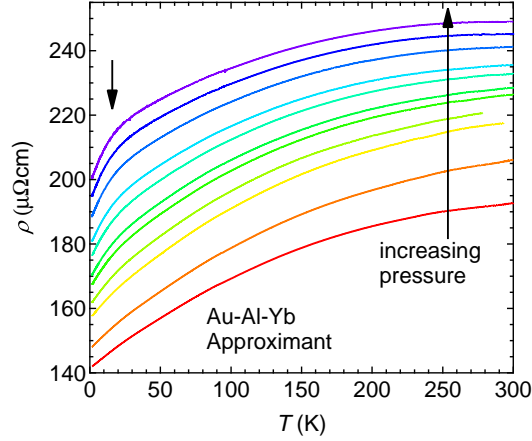


**Figure 3.2:** Temperature dependence of the electrical resistivity of the Au-Al-Yb approximant in a temperature range of  $2 \leq T \leq 300$  K at pressure  $P = 0, 0.26, 0.42, 0.61, 0.89, 0.96, 1.20, 1.51, 1.80, 2.15,$  and  $2.43$  GPa. The arrow denotes a bend-like “anomaly”.

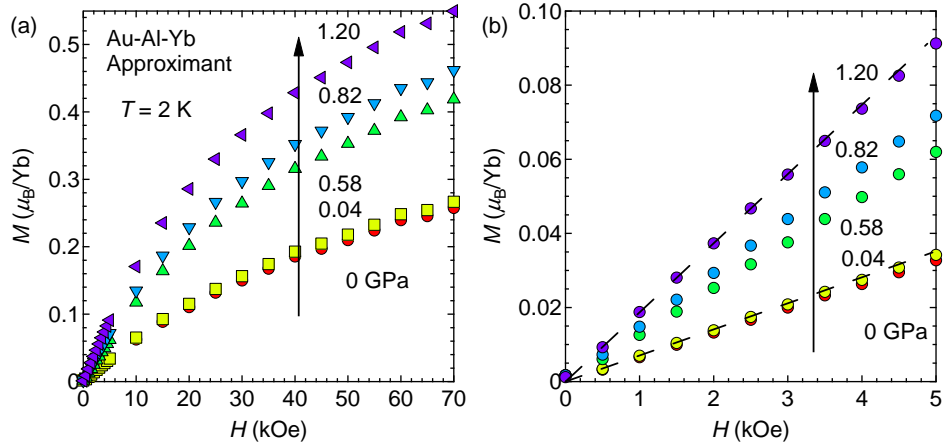
### 3.3.2 Dc magnetization under pressure

Figure 3.3 shows the magnetic field dependence of the magnetization  $M$  of the Au-Al-Yb approximant under pressure.  $M$  is linear in  $H$  up to about 3 kOe, and tends to saturate at higher fields. Figure 3.4 shows the pressure dependence of  $M/H$  of the approximant at 2 K. At a fixed field,  $M$  increases with pressure. By fitting the  $M/H$  data to Eq. 2.1, we obtain the following values:  $a = 0.0365 \pm 0.0008$ ,  $b = 0.056 \pm 0.001$ , and  $n = 0.94 \pm 0.04$ .

### 3.3.3 Magnetic susceptibility of the Au-Al-Yb approximant under hydrostatic pressure

We calibrate the ac susceptibility in a similar way to the previously mentioned method, see section 2.3. Figure 3.5 shows the temperature dependence of the ac magnetic susceptibility of the Au-Al-Yb approximant under dc magnetic field  $H$  and hydrostatic pressure  $P$ . The low-temperature susceptibility for  $H = 0$  strongly increases with pressure, whereas the application of the dc field suppresses this increase. At  $P = 2.39$  and  $2.79$  GPa, a peak structure is formed at  $T_g \simeq 100$  mK for  $H = 0$ . We discuss a possible origin of this peak structure below.

On the basis of the results as shown above (see section 1.4.2), we assume the following modified Curie–Weiss relation for  $H = 0$  except in a



**Figure 3.3:** (a) Magnetic field dependence of the magnetization of the Au-Al-Yb approximant under pressure. (b) Magnetization curves below 5 kOe. The dashed lines are guides to the eyes.

temperature region near  $T_g$ ;

$$\chi(T)^{-1} = T^\gamma/C + \chi(0)^{-1}. \quad (3.1)$$

Here,  $\gamma$  is the critical exponent. The traditional Curie–Weiss plot where  $1/\chi$  is a straight line as a function of  $T$  is replaced by a plot where  $1/\chi$  is a straight line as a function of  $T^\gamma$  with the slope  $1/C$  (where  $C$  is the Curie constant) and the vertical-axis intercept  $\chi(0)^{-1}$ . This straight-line feature is confirmed in Fig. 3.6(a) over a temperature range between about 85 mK (the base temperature of the experiment) and about 800 mK. Assuming the exponent  $\gamma$  as a free parameter, we obtain  $\gamma = 0.50 \pm 0.05$  at ambient pressure and  $\gamma = 0.50 \pm 0.01$  at  $P = 1.96$  GPa. This means that the exponent  $\gamma$  does not depend on pressure within the experimental accuracy. In contrast, the intercept  $\chi(0)^{-1}$  (that measures the distance from QCP) approaches zero with increasing pressure toward about 2.0 GPa. This observation is more clearly seen in Fig. 3.6(b):  $1/\chi(0)$  steeply decreases with increasing pressure and vanishes at around 2 GPa, suggesting the emergence of the QCP there. On the other hand,  $1/\chi(0)$  of the quasicrystal is independent of pressure with keeping  $1/\chi(0) \sim 0$ . As a result, the approximant shows qualitatively different response from the quasicrystal with respect to the application of hydrostatic pressure.

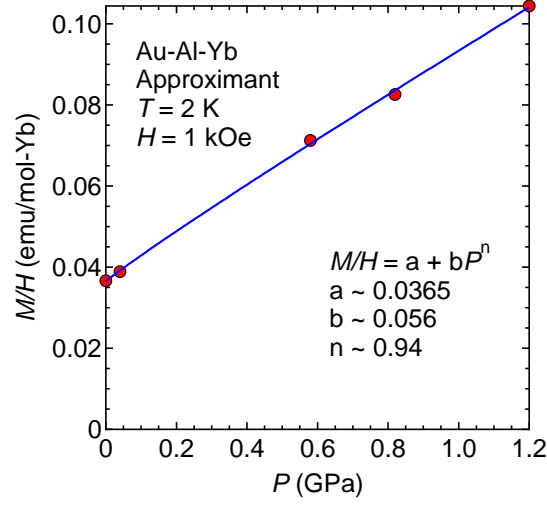


**Figure 3.4:** Pressure dependence of the magnetic susceptibility of the approximant at 2 K. The blue solid line shows the best fitted curve.

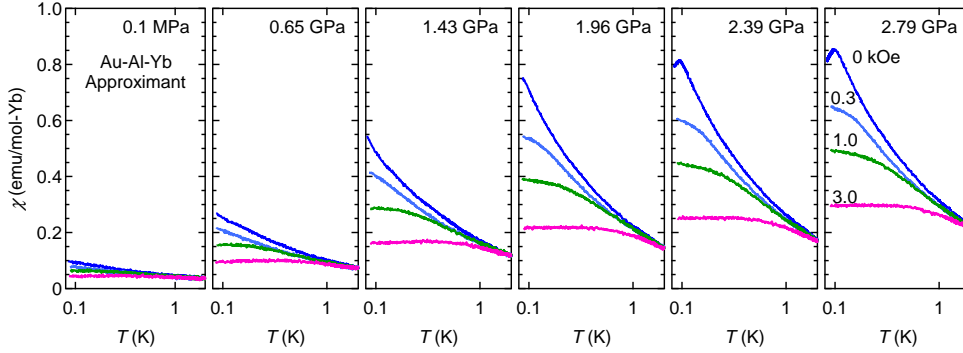


**Figure 3.5:** Temperature dependence of the ac magnetic susceptibility of the Au-Al-Yb approximant in a temperature range of  $0.08 \leq T \leq 2 \text{ K}$  at pressures indicated in each panel. Applied dc magnetic fields are denoted in the figure of  $P = 2.79 \text{ GPa}$ .

### 3.3.4 Nature of the magnetic ordered phase above 2 GPa: an antiferromagnetically long-range ordered phase or a spin glass like short-range ordered phase

As shown in the previous section, the magnetic susceptibility of the approximant shows an anomaly at around 100 mK at pressures of 2.39 and 2.79 GPa (see Fig. 3.5). The anomaly is naturally ascribed to the onset of either

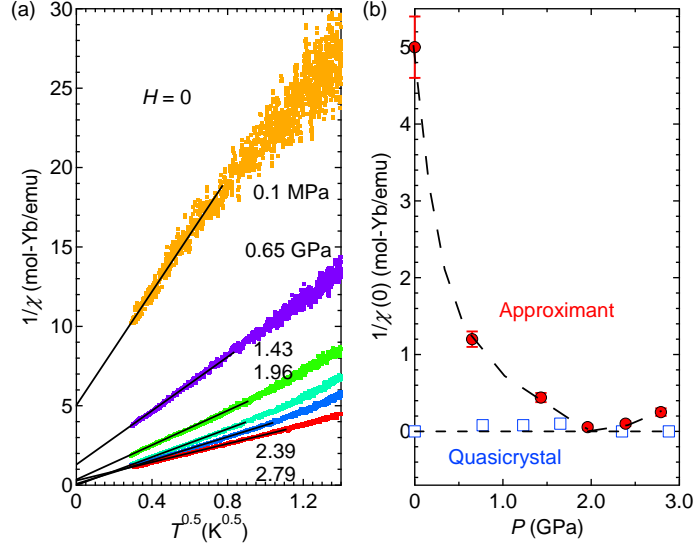


**Figure 3.6:** (a) Plot of  $1/\chi$  vs  $T^{0.5}$  of the Au-Al-Yb approximant at  $H = 0$  under pressure. The straight line indicates the extrapolation to zero temperature to evaluate  $1/\chi(0)$ . (b) Pressure dependence of  $1/\chi(0)$  at  $H = 0$  of the approximant and the quasicrystal.

an antiferromagnetically long-range order or a spin glass like short-range order. To elucidate the long-range or short-range ordered state, it is useful to measure the nonlinear susceptibility  $\chi_2$  defined as follows,

$$\chi_{ac}(H) = \frac{dM}{dH} = \chi_0 + \chi_2 H^2 + \dots \quad (3.2)$$

Here,  $\chi_{ac}$ ,  $M$ ,  $\chi_0$ , and  $\chi_2$  are the ac susceptibility, the magnetization, the linear susceptibility, and the nonlinear susceptibility, respectively. Figure 3.7 schematically shows the temperature dependence of  $\chi_2$  around an antiferromagnetic ordering temperature  $T_N$  (a) and a spin-glass freezing temperature  $T_g$  (b) [19]. In the case of the antiferromagnetic order,  $-\chi_2$  shows no divergence and a sign change at  $T_N$ . In the case of the spin-glass transition, on the other hand,  $-\chi_2$  diverges at both sides of  $T_g$ . In this thesis,  $\chi_2$  was evaluated as the initial slope of the  $\chi_{ac}$  vs  $H^2$  curve (see Fig. 3.8), assuming that  $\chi_{ac}$  is proportional to  $H^2$  up to 300 Oe, i.e., assuming the following equation,

$$\chi_2(T) = \frac{\chi_{ac}(T, H) - \chi_{ac}(T, 0)}{H^2}. \quad (3.3)$$

Thus obtained results are plotted in Fig. 3.9. Note that  $-\chi_2$  forms a positive peak around  $T_g$  at which the linear susceptibility peaks. This strongly

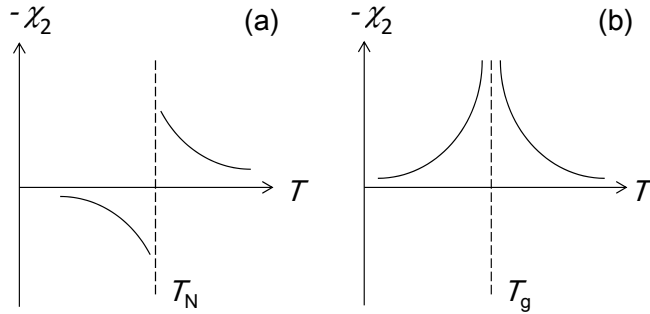


**Figure 3.7:** Schematic illustration of the nonlinear susceptibility of an antiferromagnetic order (a) and a spin-glass-like short-range order (b) as a function of temperature.  $T_N$  and  $T_g$  indicate a Néel temperature and a freezing temperature, respectively.

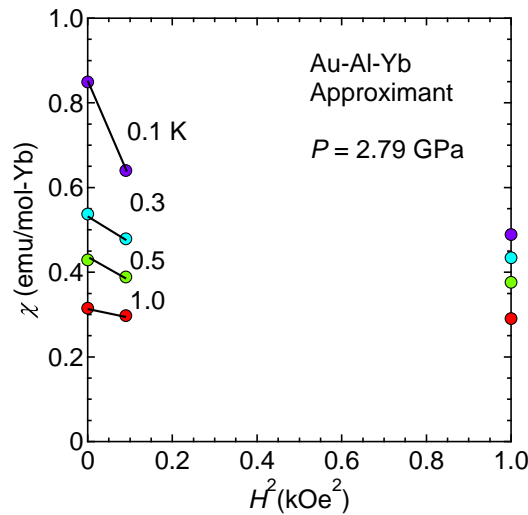


**Figure 3.8:** Plot of  $\chi_{ac}$  vs  $H^2$  at 2.79 GPa. The nonlinear susceptibility  $\chi_2$  was obtained as the slope of the solid line.

suggests that the ordering is of short-range ordered nature.

Figure 3.10 shows the temperature dependence of the ac magnetic susceptibility measured at several frequencies of the modulation field. We clearly observe a peak at low temperature as indicated by the arrow although it is not obvious at  $f = 3003$  Hz. The peak slightly but definitely shifts to higher temperatures as the frequency  $f$  increases. This result was

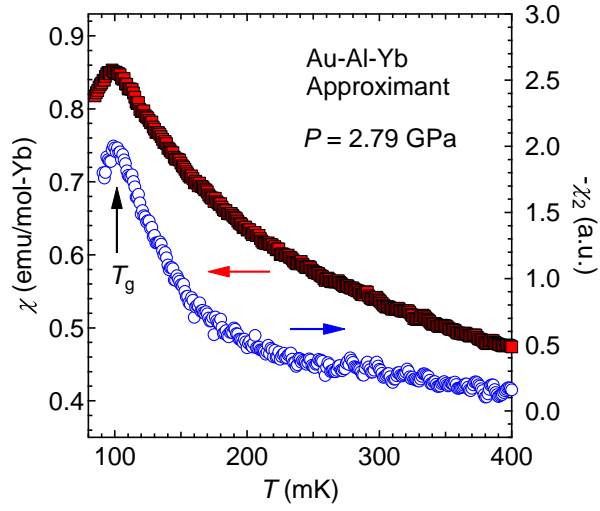


**Figure 3.9:** Temperature dependence of the magnetic susceptibility (left axis) and the nonlinear susceptibility (right axis) of the Au-Al-Yb approximant at 2.79 GPa.

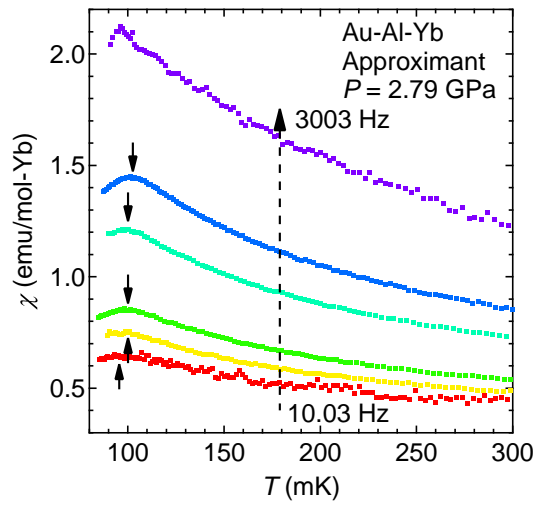


**Figure 3.10:** Temperature dependence of the magnetic susceptibility of the Au-Al-Yb approximant at 2.79 GPa, measured at different applied frequency  $f = 10.03, 50.03, 100.3, 500.3, 1003,$  and  $3003$  Hz. The arrow indicates the freezing temperature  $T_g$ .

fitted to the following equation (Vogel-Fulcher law),

$$f = f_0 \exp \left[ -\frac{W}{k_B(T_g - T_0)} \right]. \quad (3.4)$$

Here,  $f_0$ ,  $W$ , and  $k_B$  are the characteristic frequency, the activation energy, and the Boltzmann constant, respectively.  $T_0$  is called ‘ideal glass’ temperature although its physical meaning is unclear. From the results shown in Fig. 3.11, we obtain the following values:  $f_0 = 10^{13}$  Hz,  $W/k_B = 760 \pm 100$  mK, and  $T_0 = 68 \pm 4$  mK. This finding of the Vogel-Fulcher law gives a supporting evidence for the interpretation of the glass-transition at  $T_g$ .

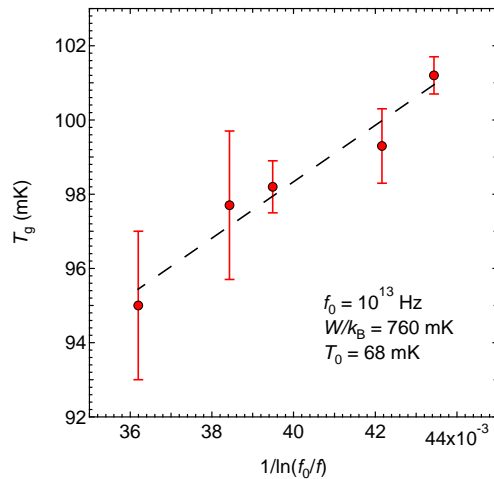


**Figure 3.11:** Variation of the freezing temperature  $T_g$  with  $1/\ln(f_0/f)$ , with  $f_0 = 10^{13}$  Hz. The dashed line is a guide to the eyes.

### 3.3.5 Origin of the quantum criticality of the Au-Al-Yb approximant

Let us discuss again a possible origin of the quantum criticality. As presented above, the uniform susceptibility shows the power-law divergence with the critical index  $\gamma \simeq 0.5$  at  $P = P_c$ . This divergence cannot be understood from the conventional magnetic QCP because the high-pressure magnetic state is not ferromagnetic but spin-glass like. Instead, the divergence with the above critical index can be explained by the critical valence fluctuation model proposed by Watanabe and Miyake [17]. It may be important to note here that the valence fluctuation between  $\text{Yb}^{2+}$  and  $\text{Yb}^{3+}$  was observed in the approximant by X-ray absorption experiments [13] and photoemission

experiments [14] (see section 1.3). Therefore, the critical valence model is likely to be a most probable model.

### 3.3.6 $P$ - $T$ phase diagram of the Au-Al-Yb approximant

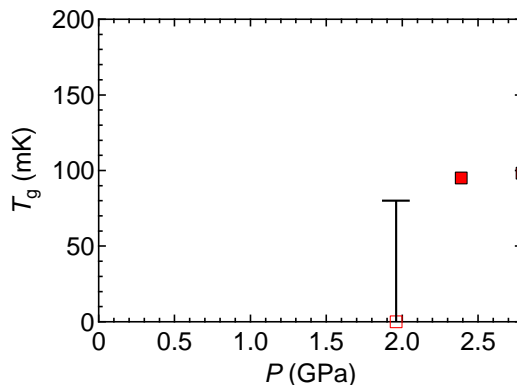


**Figure 3.12:** Pressure dependence of the freezing temperature  $T_g$ . The lowest temperature of the present measurement is 80 mK.

Let us discuss the  $P$ - $T$  phase diagram of the Au-Al-Yb approximant. In the previous section, we show that the QCP is located at  $P_c$ . At  $P > P_c$ , the approximant undergoes a spin-glass-like short-range ordering at about 100 mK. Figure 3.12 shows the pressure dependence of the freezing temperature  $T_g$ . Unfortunately, we could not determine the critical pressure where  $T_g$  comes down to zero because  $T_g$  is very low. It remains unclear if there is a QCP of the glass transition. Here, it should be noted that this QCP (if present) is distinguished from the aforementioned QCP presumably due to the critical valence fluctuation. From these results, we suggest some possible  $P$ - $T$  phase diagrams (see Figs. 3.13 (a)-(d)). In 3.13 (a), there are two QCPs, one is the QCP of the magnetic origin and the other is the QCP of the critical valence fluctuation. The two characteristic lines (the valence crossover line  $T_V^*$  and the magnetic transition  $T_g$ ) are crossing each other. In Fig. 3.13 (b), these two QCPs coincide with each other. In Fig. 3.13 (c), there are two QCPs again as in Fig. 3.13 (a), but the  $T_V^*$  and  $T_g$  lines do not cross. In Fig. 3.13 (d), the valence fluctuation and the magnetic fluctuation suppress each other, resulting in the onset of the first order transition. It remains open which phase diagram is realized here. We need further study to resolve this problem.

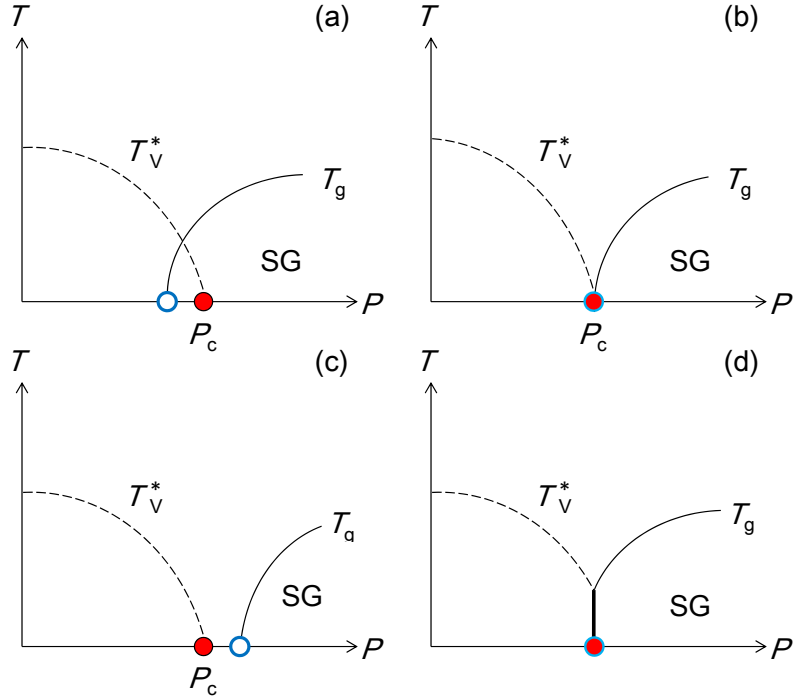


**Figure 3.13:** (a) - (d) Schematic  $P$ - $T$  phase diagrams of the Au-Al-Yb approximant.  $T_V^*$ ,  $T_g$ ,  $P_c$ , and SG indicate a hypothetical characteristic temperature that is related to valence crossover, a freezing temperature, a critical pressure at which the magnetic susceptibility diverges, and a spin-glass-like short-range ordered state, respectively. A blue open circle and red closed circle indicate the QCP of the spin glass transition and critical valence fluctuation, respectively.

### 3.3.7 Chemical pressure effect on the Au-Al-Yb approximant: valence change driven by constituent element substitution

The metal alloys  $\text{Au}_{44}\text{Ga}_{41}\text{Yb}_{15}$  and  $\text{Ag}_{47}\text{Ga}_{38}\text{Yb}_{15}$  are members of the 1/1 approximant to the Tsai-type quasicrystal [20]. Figure 3.14 shows the temperature dependence of the magnetic susceptibilities of the Au-Al-Yb, Au-Ga-Yb, and Ag-Ga-Yb approximants. We note that the magnetism disappears by substituting Ga for Al. This result suggests that the substitution of Ga for Al corresponds to the negative chemical pressure and the Au-Al-Yb system is located near the border of the divalent and trivalent states of the Yb ion.

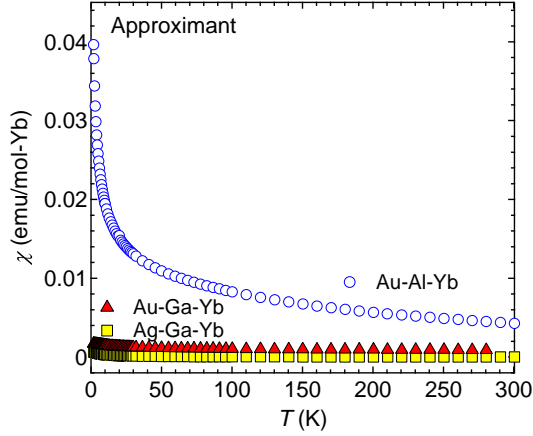


**Figure 3.14:** Temperature dependence of the magnetic susceptibilities of the Au-Al-Yb, Au-Ga-Yb, and Ag-Ga-Yb approximants. The magnetization was measured at  $H = 1, 0.1,$  and  $5$  kOe for the Au-Al-Yb, Au-Ga-Yb, and Ag-Ga-Yb approximants, respectively.

### 3.4 Summary

We measured the magnetic susceptibility of the Au-Al-Yb approximant under hydrostatic pressure. The low-temperature susceptibility increases with pressure and diverges toward zero temperature at  $P_c \simeq 2$  GPa. This means the presence of the QCP at  $P_c$ . At pressures above  $P_c$ , the spin-glass like short-range ordered state emerges at a low temperature ( $T_g \sim 100$  mK). The pressure effect observed here resembles that of the heavy fermion crystals, but it is completely different from that of the quasicrystal. The difference between the quasicrystal and the approximant seems to be naturally ascribed to the presence/absence of the quasiperiodicity.

# Chapter 4

## Discussion

### 4.1 Introduction

As presented in the previous chapters, the unconventional quantum criticality of the quasicrystal is robust against the application of the hydrostatic pressure, whereas the approximant shows the pressure-driven quantum criticality as in the conventional heavy fermion crystals. In this chapter, we discuss the origin of the difference in the pressure effect between the quasicrystal and the approximant. Indeed, the most probable origin is the presence/absence of the quasiperiodicity. We also discuss the origin of the unusual quantum criticality, although the possibility of the critical valence fluctuation was already suggested in the preceding chapters. To confirm one direction, we discuss the so-called  $T/H$  scaling.

### 4.2 Origin of the difference in the pressure effect between the Au-Al-Yb quasicrystal and the approximant

Let us discuss the origin of the difference in the pressure effect between the Au-Al-Yb quasicrystal and approximant. As mentioned in the previous chapters, the quasicrystal shows the unconventional quantum criticality with the unusual critical indices and does the robustness against the application of pressure, which results in the  $P$ - $T$  phase diagram as schematically shown in Fig. 4.1 (a). On the other hand, the approximant shows the pressure-driven quantum criticality (see Fig. 4.1 (b)), which is characterized by the same critical index as for the quasicrystal. If we look at the local geometric structure, the quasicrystal and the approximant have the similar structure. Therefore, the chemical disorder contained in the cluster is not the origin of

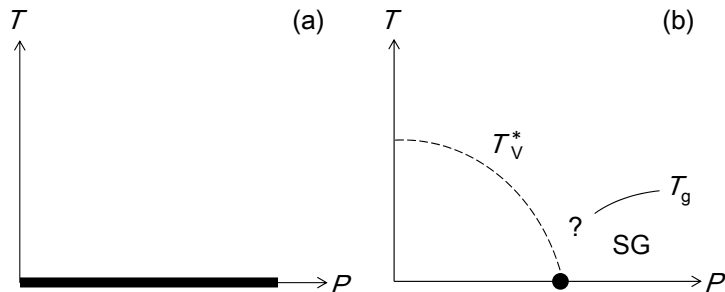


**Figure 4.1:** Schematic  $P - T$  phase diagrams of the Au-Al-Yb quasicrystal (a) and the approximant (b). The thick line in (a) indicates “a collection of QCPs”, which may be called the quantum critical line. The closed circle in (b) indicates the QCP.  $T_V^*$  is a hypothetical characteristic temperature that is related to valence crossover.  $T_g$  and SG indicate a freezing temperature and a spin-glass like short-range ordered state, respectively.

the difference. On the other hand, if we look at the overall structure, the atomic arrangement (i.e., the quasiperiodicity/periodicity) is different between them. Therefore, it is reasonable to ascribe difference in the pressure effect to the quasiperiodicity/periodicity.

### 4.3 $T/H$ scaling of the Au-Al-Yb quasicrystal and the approximant

Let us discuss the scaling relation in the Au-Al-Yb quasicrystal and the approximant. The scaling is a strong method to determine the critical exponent and to study the origin of QCP. First, we examine the scaling properties of the ac susceptibility  $\chi_{ac} = \frac{dM}{dH}$ . Let us start from the following uniform and static susceptibility that was deduced from the generalized susceptibility proposed for  $\text{CeCu}_{6-x}\text{Au}_x$  by Schröder *et al.*, [21]

$$\begin{aligned} \chi^{-1}(H, T) &= \frac{1}{C} \left[ \frac{1}{k_B^\alpha} ((k_B T)^2 + (g\mu_B H)^2)^{\alpha/2} + \theta^\alpha \right] \\ &= \frac{1}{C} \eta \left( \frac{H}{T} \right) T^\alpha + \frac{1}{C} \theta^\alpha, \end{aligned} \quad (4.1)$$

where  $k_B$ ,  $g$ ,  $\mu_B$ , and  $\theta$  are the Boltzmann constant, the effective  $g$ -factor, the Bohr magneton, and the Weiss temperature, respectively.  $\eta$  is a scaling function of the ratio  $H/T$  only and equal to 1 for  $H/T = 0$ . The power index  $\alpha$  was found to be 0.75 for  $\text{CeCu}_{6-x}\text{Au}_x$ . For the Au-Al-Yb quasicrystal

and the approximant, we obtain  $\alpha = 0.55 \sim 0.6$  and  $0.5$ , respectively, by comparing Eq. 4.1 with the phenomenologically determined Eq. 3.1. (Note that  $\eta = 1$  for  $H = 0$  as mentioned above.) At the QCP where  $\chi(0)^{-1} = \theta^\alpha/C = 0$ , we have the scaling relation

$$\chi T^\alpha = C\eta^{-1}, \text{ at QCP.} \quad (4.2)$$

We plot  $\chi T^\alpha$  of the quasicrystal and the approximant as functions of  $H/T$  in Figs. 4.2 and 4.3, respectively. In Fig. 4.2, we find that all the data fall on a single curve, meaning that the scaling relation Eq. 4.2 holds at all pressures in the quasicrystal. On the other hand, in Fig. 4.3, we find that only the data of  $P = 1.96$  GPa close to  $P_c$  collapse on a single curve. As a result, we note again that the quantum criticality of the quasicrystal survives under pressure.

Defining  $X$  as

$$X^{-1} = \chi^{-1} - \frac{\theta^\alpha}{C}, \quad (4.3)$$

we obtain the similar scaling relation

$$XT^\alpha = C\eta^{-1}. \quad (4.4)$$

Equation 4.4 also holds because the data even at  $P \neq P_c$  fall on a single curve, as seen in Fig. 4.4. Taking into account the fact that  $C$  depends on pressure (see Fig. 3.6(a)), we plot  $XT^{0.5}/C$  in Fig. 4.5(c); although the ambient pressure data scatter owing to their small susceptibility, all pressure data taken here fall on a single curve, which manifests that  $XT^{0.5}/C$  is a function of  $H/T$  only.

Equation (4.4) is confirmed more quantitatively. According to the asymptotic form of the scaling function  $\eta^{-1}$ ,

$$\eta^{-1} \left( \frac{H}{T} \right) \sim \begin{cases} 1 - \frac{1}{4} \left( \frac{g\mu_B H}{k_B T} \right)^2, & \text{for } T \gg H, \\ \left( \frac{g\mu_B H}{k_B T} \right)^{-1/2}, & \text{for } T \ll H. \end{cases} \quad (4.5)$$

The data shown in Fig. 4.5 saturate at unity in the non-Fermi liquid limit ( $H/T \ll 1$ ), while in the opposite limit of Fermi liquid ( $H/T \gg 1$ ), they decrease linearly with increasing  $H/T$ . This indicates that the magnetic field drives the system to the Fermi liquid regime.

Next, we discuss that the unusual exponent  $\alpha = 0.5$  obtained above can be deduced from the following low-temperature free energy, which was proposed for the analysis of the quantum criticality of  $\beta$ -YbAlB<sub>4</sub> by Matsumoto *et al.*, [22]

$$F = -\frac{1}{(k_B \tilde{T})^{1/2}} \left[ (g\mu_B H)^2 + (k_B T)^2 \right]^{3/4}, \quad (4.6)$$

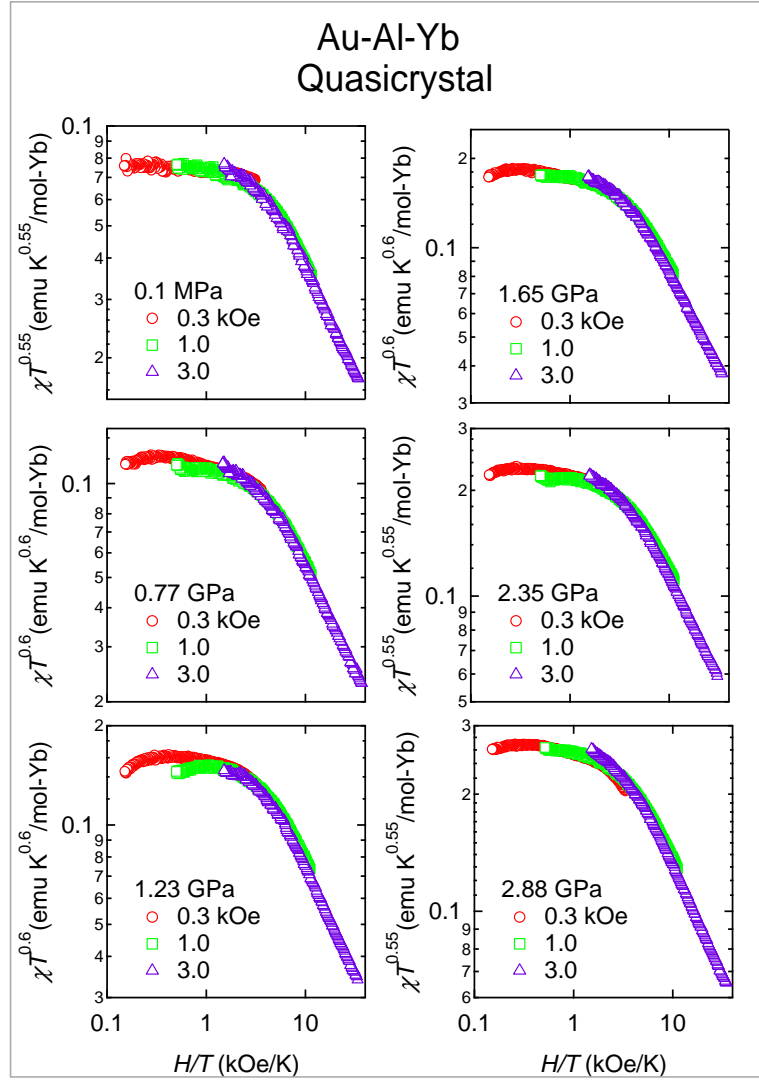


**Figure 4.2:**  $H/T$  scaling of the Au-Al-Yb quasicrystal. The scaling behavior was observed at all  $P$ . This indicates that the quantum criticality survives under pressure.

where  $\tilde{T}$  is a characteristic temperature. By differentiating  $F$  with respect to  $H$ , we obtain the ac susceptibility  $\chi = dM/dH$  and the dc susceptibility

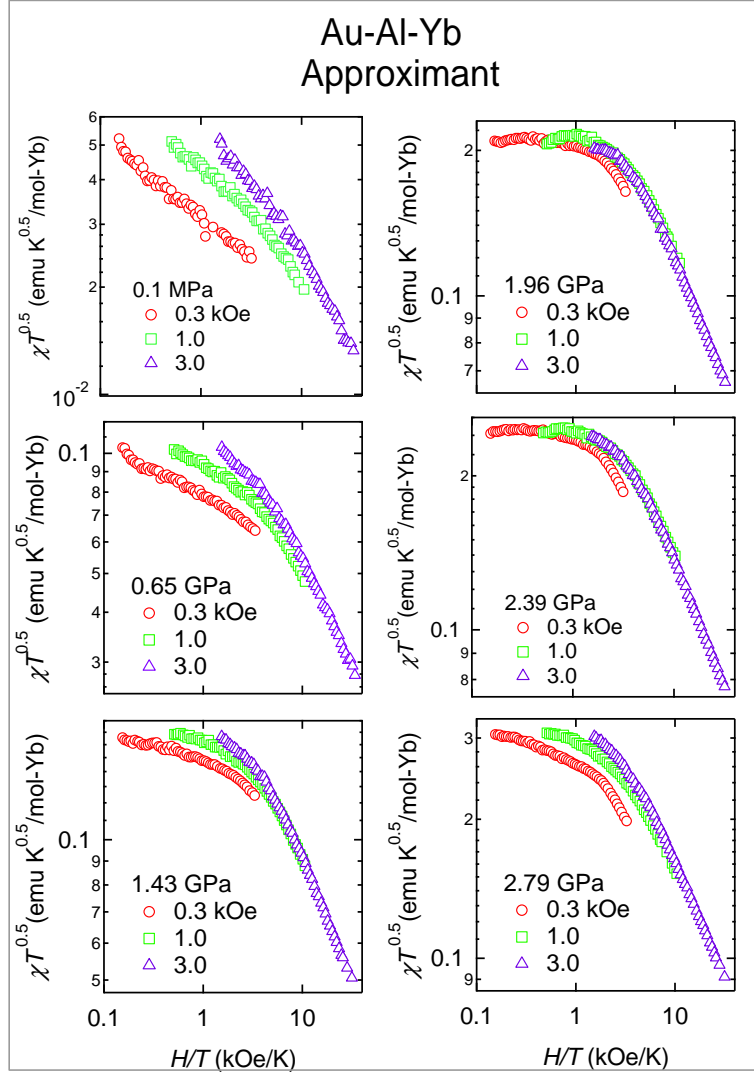


**Figure 4.3:**  $H/T$  scaling of the Au-Al-Yb approximant. The scaling behavior observed at  $P = 1.96$  GPa ( $\approx P_c$ ) becomes less evident as  $P$  moves away from  $P_c$ .

$M/H$  (where  $M$  is a magnetization) as

$$\chi(T, H)T^{1/2} = \psi\left(\frac{H}{T}\right), \quad \text{for } H \geq 0, \quad (4.7)$$

$$\frac{M}{H}H^{1/2} = \varphi\left(\frac{T}{H}\right), \quad \text{for } H > 0, \quad (4.8)$$

where  $\psi$  and  $\varphi$  are scaling functions, and  $\psi = \frac{3}{2} \frac{(g\mu_B)^2}{k_B \tilde{T}^{1/2}}$  for  $H = 0$ . Equation (4.7) is equivalent to Eq. (4.2) when  $C\eta^{-1} = \psi$ , and a comparison of Eq. (4.7) with Eq. (4.1) yields  $\alpha = 0.5$ .

Then, we test the scaling relation Eq. (4.8) for the dc magnetization using data taken at high temperatures ( $2 \text{ K} \lesssim T \lesssim \text{room temperature}$ ) and high dc fields ( $H \lesssim 70 \text{ kOe}$ ) (see Figs. 4.6 (a) and (b)). (We used the ambient-pressure data instead of the high-pressure one because the high-pressure magnetization contains a non-negligible contribution from the pressure cell and it was difficult to accurately separate the sample magnetization from the total magnetization.) In both of the quasicrystal and the approximant, for  $T/H > 10$  (i.e.,  $T > 10 \text{ K}$  for  $H = 1 \text{ kOe}$ ), we find a deviation from the expected behavior (denoted by the thin line) from the asymptotic form

$$\varphi\left(\frac{T}{H}\right) \sim \frac{3(g\mu_B)^{3/2}}{2(k_B \tilde{T})^{1/2}} \left(\frac{k_B T}{g\mu_B H}\right)^{-1/2}, \text{ for } T \gg H. \quad (4.9)$$

This may be ascribed to the crystal field effect because the  $4f$  electrons are localized at high temperatures as evidenced by the conventional Curie–Weiss behavior in  $\chi(T)$  [2, 12]. It is now clear that the  $T/H$  scaling holds (except in the very high temperature region) in the quasicrystal and the approximant, like in  $\text{CeCu}_{6-x}\text{Au}_x$  and  $\beta\text{-YbAlB}_4$ . In all four systems, therefore, the critical field  $H_c$  of the quantum phase transition is zero because a finite  $H_c$  would require that the argument of the scaling functions is the ratio  $T/|H - H_c|$  [22], and further that these systems may have the same origin for the unusual non-Fermi liquid behavior. This may lead to a similar  $H$ - $T$  phase diagram for those systems, in contrast to the  $P$ - $T$  phase diagram that strongly depends on the system as demonstrated in Fig. 4.1; for  $\text{CeCu}_{5.8}\text{Au}_{0.2}$  and  $\beta\text{-YbAlB}_4$ , see Refs. [23] and [24], respectively.

## 4.4 Origin of the unusual quantum criticality

Let us discuss the origin of the quantum criticality of the Au–Al–Yb approximant and the quasicrystal. First, we consider the approximant. There are two possible origins of the quantum criticality in the approximant. One is due to the QCP of the glass transition. However, this possibility is presumably excluded because the uniform susceptibility will not diverge at  $T_g = 0$ . The second possibility is due to the critical valence fluctuation. The divergence of the uniform susceptibility with the critical index  $\gamma \simeq 0.5$  can be explained by the critical valence fluctuation model proposed by Watanabe and Miyake [17]. We note that the valence fluctuation between  $\text{Yb}^{2+}$  and  $\text{Yb}^{3+}$  was observed in the approximant by X-ray absorption experiments [13]

and photoemission experiments [14] (see section 1.4.2). From these results, we consider that this possibility seems most probable. Next, we consider the quasicrystal. Since we have detected no magnetic ordering in contrast to the approximant, the magnetic origin is unambiguously excluded. Then, the second possibility remains to be a possible origin. As a result, for both the quasicrystal and the approximant, the critical valence fluctuation is most likely to be the origin of the unusual low-temperature properties.

## 4.5 Summary

The  $P$ - $T$  phase diagram is very different between the quasicrystal and the approximant. However, the critical behavior and the  $H/T$  scaling of the quasicrystal are very similar to those of the approximant at  $P = P_c$ . Furthermore, the similar criticality and the scaling are applicable to  $\text{CeCu}_{6-x}\text{Au}_x$  and  $\beta\text{-YbAlB}_4$ . This suggests that all these systems have the common origin of the unusual low-temperature properties.

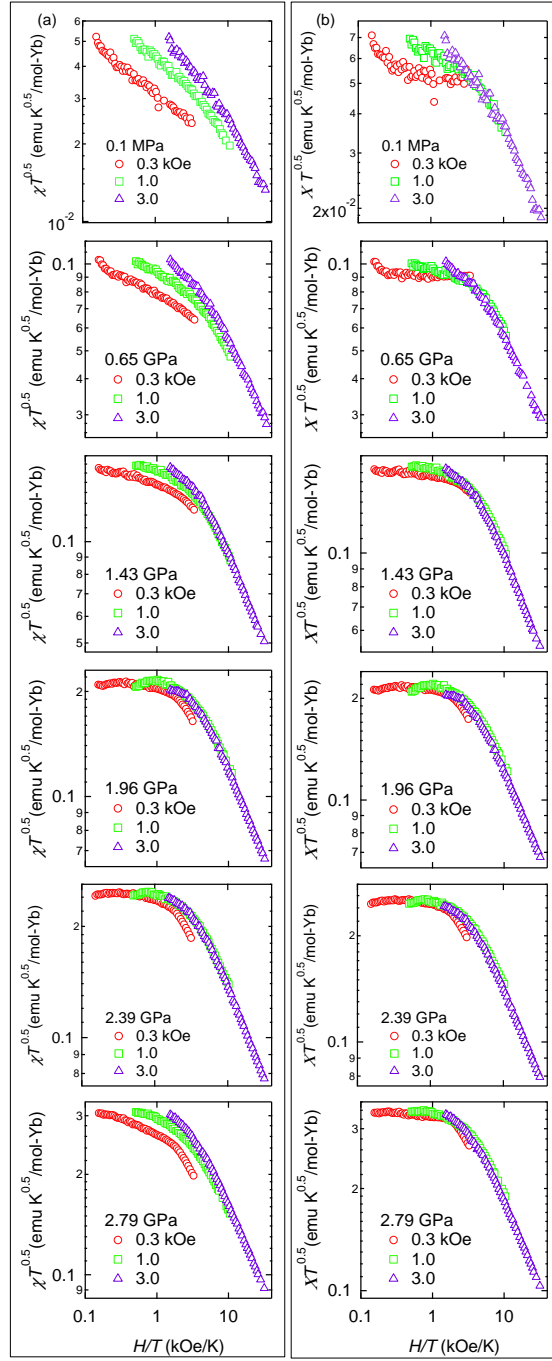


**Figure 4.4:**  $H/T$  scaling of the Au-Al-Yb approximant. The vertical axis denotes (a)  $\chi T^{0.5}$  and (b)  $X T^{0.5}$ . (a) The scaling behavior observed at  $P = 1.96$  GPa ( $\simeq P_c$ ) becomes less evident as  $P$  moves away from  $P_c$ . (b) The critical component  $X$  satisfies the scaling relation even for  $P \neq P_c$ .

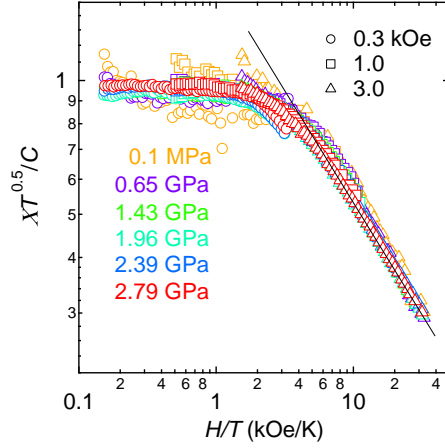


**Figure 4.5:** Plot of  $XT^{0.5}/C$  as a function of  $H/T$  of the Au-Al-Yb approximant. All data fall on a single curve. The straight line indicates the Fermi liquid limit of the scaling function  $\eta^{-1}$ .

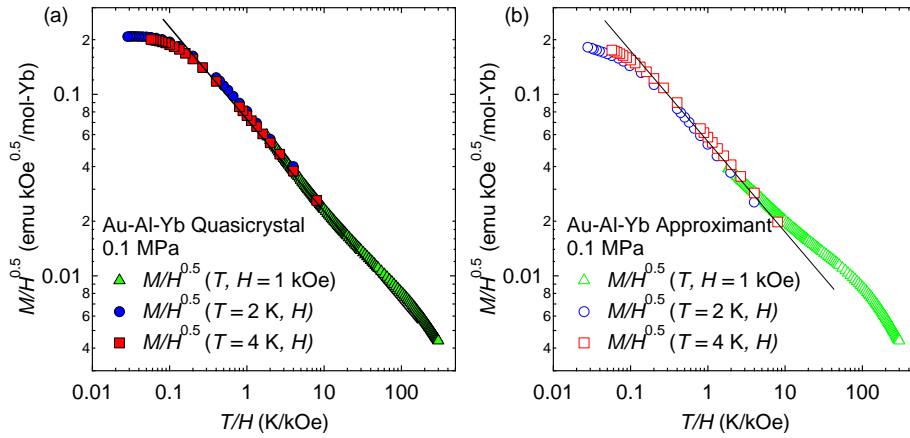


**Figure 4.6:**  $T/H$  scaling of dc susceptibility,  $(M/H)H^{0.5}$ , of the Au-Al-Yb quasicrystal (a) and the approximant (b), in a temperature interval between 2 K and room temperature. Note that the horizontal axis denotes  $T/H$ , instead of  $H/T$  in Figs. 4.2 and 4.3. Triangles indicate a temperature-sweep experiment, and circles and squares indicate a dc-field-sweep experiment at  $T = 2$  and 4 K, respectively.



## Chapter 5

# Summary

The Au-Al-Yb quasicrystal shows the unconventional quantum criticality without tuning. The magnetic susceptibility and the specific heat diverges as  $T \rightarrow 0$ , with unusual critical indices. By comparing the critical behavior of the magnetic susceptibility and the specific heat with the critical valence fluctuation theory and by remembering that there is no ferromagnetic phase nearby, we conclude that the most probable origin of the criticality is the critical valence fluctuation. Actually, the valence fluctuation between  $\text{Yb}^{2+}$  and  $\text{Yb}^{3+}$  in the quasicrystal was observed by X-ray absorption and photoemission experiments. Since the critical index of the quasicrystal is similar to that of the approximant, the same model seems applicable to the approximant. As a result, the critical valence fluctuation seems responsible for both the quasicrystal and the approximant.

In order to investigate the pressure effect on the quantum criticality of the Au-Al-Yb quasicrystal, we measured the magnetic susceptibility of the quasicrystal under hydrostatic pressure. We found that the magnetic susceptibility diverges under pressure, with the same critical index as the ambient pressure. This means that the quantum criticality of the quasicrystal is robust against the application of hydrostatic pressure. This leads to very unusual  $P$ - $T$  phase diagram, in remarkably contrasted to the diagram of the heavy fermion crystals. We further studied the magnetic properties of the Au-Al-Yb approximant under hydrostatic pressure to make a comparison with those of the quasicrystal. We found that the magnetic susceptibility of the approximant diverges toward  $T \rightarrow 0$  at  $P_c \sim 2$  GPa. This means that there is a quantum critical point at  $P_c$ . At  $P > P_c$ , the spin-glass-like short-range ordered state emerges below  $T_g \sim 100$  mK. These results clearly indicate that the pressure effect on the approximant is essentially different from that of the quasicrystal. Remembering that the difference in the geometric structure between the quasicrystal and the approximant

is the presence/absence of the quasiperiodicity, the origin of the difference in the pressure effect is reasonably ascribed to the difference in the presence/absence of the quasiperiodicity. As a result, the  $P$ - $T$  phase diagram is unique to the quasicrystal.

Finally, we study the  $T/H$  scaling. We found that the quasicrystal and the approximant satisfy the  $T/H$  scaling similar to  $\text{CeCu}_{6-x}\text{Au}_x$  and  $\beta$ - $\text{YbAlB}_4$ . This means that there is no critical field  $H_c$  for these materials, and further suggest that these three systems may have the same origin for the unusual non-Fermi liquid behavior.

# Bibliography

- [1] T. Ishimasa, Y. Tanaka, and S. Kashimoto: *Phil. Mag.* **91**, 4218 (2011).
- [2] K. Deguchi, S. Matsukawa, N. K. Sato, T. Hattori, K. Ishida, H. Takakura, and T. Ishimasa: *Nat. Mater.* **11**, 1013 (2012).
- [3] O. Trovarelli, C. Geibel, S. Mederle, C. Langhammer, F. M. Grosche, P. Gegenwart, M. Lang, G. Sparn, and F. Steglich: *Phys. Rev. Lett.* **85**, 626 (2000).
- [4] S. Nakatsuji, K. Kuga, Y. Machida, T. Tayama, T. Sakakibara, Y. Karaki, H. Ishimoto, S. Yonezawa, Y. Maeno, E. Pearson, G. G. Lonzarich, L. Balicas, H. Lee, and Z. Fisk: *Nat. Phys.* **4**, 603 (2008).
- [5] V. Elser: *Acta Cryst. A* **42**, 36 (1986).
- [6] A. I. Goldman and R. F. Kelton: *Rev. Mod. Phys.* **65**, 213 (1993).
- [7] K. Satoh, T. Fujita, Y. Maeno, Y. Onuki, and T. Komatsubara: *J. Phys. Soc. Jpn.* **58**, 1012 (1989).
- [8] N. Sato, S. Kunii, I. Oguro, T. Komatsubara, and T. Kasuya: *J. Phys. Soc. Jpn.* **53**, 3967 (1984).
- [9] T. Moriya: *Spin Fluctuations in Itinerant Electron Magnetism* (Springer, 1985).
- [10] A. P. Tsai, J. Q. Guo, E. Abe, H. Takakura, and T. J. Sato: *Nature* **408**, 537 (2000).
- [11] H. Takakura, C. P. Gómez, A. Yamamoto, M. De Boissieu, and A. P. Tsai: *Nat. Mater.* **6**, 58 (2007).
- [12] S. Matsukawa, K. Tanaka, M. Nakayama, K. Deguchi, K. Imura, H. Takakura, S. Kashimoto, T. Ishimasa, and N. K. Sato: *J. Phys. Soc. Jpn.* **83**, 034705 (2014).

- [13] T. Watanuki, S. Kashimoto, D. Kawana, T. Yamazaki, A. Machida, Y. Tanaka, and T. J. Sato: Phys. Rev. B **86**, 094201 (2012).
- [14] M. Matsunami, A. Chainani, M. Taguchi, M. Oura, S. Shin, T. Hajiri, S. Kimura, T. Takeuchi, K. Tamasaku, Y. Tanaka, T. Ishikawa, T. Ebihara, K. Imura, K. Deguchi, N. K. Sato, and T. Ishimasa: unpublished.
- [15] Q. Si, S. Rabello, K. Ingersent, and J. L. Smith: Nature **413**, 804 (2001).
- [16] E. Miranda, and V. Dobrosavljević: Rep. Prog. Phys. **68**, 2337 (2005).
- [17] S. Watanabe and K. Miyake: Phys. Rev. Lett. **105**, 186403 (2010).
- [18] L. D. Jennings and C. A. Swenson: Phys. Rev. **112**, 31 (1958).
- [19] S. Fujiki and S. Katsura: Prog. Theor. Phys. **65**, 1130, (1981).
- [20] S. Matsukawa, K. Tanaka, M. Nakayama, K. Deguchi, K. Imura, H. Takakura, S. Kashimoto, T. Ishimasa, and N. K. Sato: J. Phys. Soc. Jpn. **83**, 034705 (2014).
- [21] A. Schröder, G. Aeppli, R. Coldea, M. Adams, O. Stockert, H. v. Löhneysen, E. Bucher, R. Ramazashvili, and P. Coleman: Nature **407**, 351 (2000).
- [22] Y. Matsumoto, S. Nakatsuji, K. Kuga, Y. Karki, N. Horie, Y. Shimura, T. Sakakibara, A. H. Nevidomskyy, and P. Coleman: Science **331**, 316 (2011).
- [23] O. Stockert, F. Huster, A. Neubert, C. Pfleiderer, T. Pietrus, B. Will, and H. v. Löhneysen: Physica B **312-313**, 458 (2002).
- [24] T. Tomita, K. Kuga, Y. Uwatoko, P. Coleman, and S. Nakatsuji: Science **349**, 506 (2015).

# Published Work

- Journal articles

- [1] K. Deguchi, S. Matsukawa, N. K. Sato, T. Hattori, K. Ishida, H. Takakura, and T. Ishimasa:  
“Quantum critical state in a magnetic quasicrystal”  
Nat. Mater. **11**, 1013 (2012).
- [2] S. Matsukawa, K. Tanaka, M. Nakayama, K. Deguchi, K. Imura, H. Takakura, S. Kashimoto, T. Ishimasa, and N. K. Sato:  
“Valence Change Driven by Constituent Element Substitution in the Mixed-Valence Quasicrystal and Approximant Au-Al-Yb”  
J. Phys. Soc. Jpn. **83**, 034705 (2014).
- [3] K. Deguchi, M. Nakayama, S. Matsukawa, K. Imura, K. Tanaka, T. Ishimasa, and N. K. Sato:  
“Crystal Structure of Superconducting 1/1 Cubic Au-Ge-Yb Approximant with Tsai-Type Cluster”  
J. Phys. Soc. Jpn. **84**, 015002 (2015).
- [4] K. Deguchi, M. Nakayama, S. Matsukawa, K. Imura, K. Tanaka, T. Ishimasa, and N. K. Sato:  
“Superconductivity of Au-Ge-Yb Approximatns with Tsai-Type Clusters”  
J. Phys. Soc. Jpn. **84**, 023705 (2015).
- [5] M. Nakayama, K. Tanaka, S. Matsukawa, K. Deguchi, K. Imura, T. Ishimasa, and N. K. Sato:  
J. Phys. Soc. Jpn. **84**, 024721 (2015).
- [6] S. Matsukawa, K. Deguchi, K. Imura, T. Ishimasa, and N. K. Sato:  
“Pressure-Driven Quantum Criticality and  $T/H$  Scaling in the Icosahedral Au-Al-Yb Approximant”  
J. Phys. Soc. Jpn. **85**, 063706 (2016).

- Proceedings

- [1] S. Matsukawa, K. Tanaka, M. Nakayama, S. Kunikata, K. Deguchi, K. Imura, T. Ishimasa, and N. K. Sato:  
“Transport Properties of the Au-Al-Yb Quasicrystal and Approximant under Hydrostatic Pressure”  
Acta Physica Polonica A **126**, 527 (2014).  
Proceedings of the 12th International Conference on Quasicrystals.

- [2] K. Tanaka, Y. Tanaka, T. Ishimasa, M. Nakayama, S. Matsukawa, K. Deguchi, and N. K. Sato:  
 “Tsai-Type Quasicrystal and Its Approximant in Au-Al-Tm Alloys”  
*Acta Physica Polonica A* **126**, 603 (2014).  
 Proceedings of the 12th International Conference on Quasicrystals.
- [3] S. Matsukawa, K. Deguchi, K. Imura, T. Ishimasa, and N. K. Sato:  
 “Magnetic Properties of the Au-Al-Yb Approximant under Hydrostatic Pressure”  
 Proceedings of the 13th International Conference on Quasicrystals (in press).

## Presentation at International Conference

- [1] S. Matsukawa, K. Tanaka, M. Nakayama, S. Kunikata, K. Deguchi, K. Imura, T. Ishimasa, and N. K. Sato:  
 “Transport Properties of the Au-Al-Yb Quasicrystal and Approximant under Hydrostatic Pressure”  
 The 12th International Conference on Quasicrystals, Krakow, Poland, September 2013.
- [2] S. Matsukawa, M. Nakayama, T. Yamashita, K. Nobe, K. Kamiya, K. Deguchi, K. Imura, T. Ishimasa, and N. K. Sato:  
 “High pressure effect on low-temperature properties of the approximant crystal to magnetic Au-Al-Yb quasicrystal”  
 20th International Conference on MAGNETISM, Barcelona, Spain, July 2015.
- [3] S. Matsukawa, K. Deguchi, K. Imura, T. Ishimasa, and N. K. Sato:  
 “Magnetic Properties of the Au-Al-Yb Approximant under Hydrostatic Pressure”  
 The 13th International Conference on Quasicrystals, Kathmandu, Nepal, September 2016.

## Acknowledgments

I would like to express my great appreciation to many people helping this study. I first would like to appreciate Prof. Dr. Noriaki K. Sato for his great advice and support. He gave me the many opportunities for my growing up. I have learned many things about the present study from his great guidance and useful advice. I would like to thank Dr. Kazuhiko Deguchi for fruitful discussions on the experimental results and analyses. I would like to acknowledge Dr. Keiichiro Imura for fruitful advice and teaching of experimental techniques. I would like to appreciate Prof. Dr. Tsutomu Ishimasa for his great advice on the quasicrystal's structure. I would like to thank Mr. Yukinori Tanaka, Mr. Shin Yamamoto, and Mr. Katsumasa Tanaka for support of the experiments. I would like to thank Dr. Shinji Watanabe and Prof. Dr. Kazumasa Miyake for valuable discussions. I wish to express my gratitude to all the members in the laboratory of Magnetism for providing the good environments for my research. I would like to thank the staffs of Low Temperature Laboratory for providing the liquid helium and nitrogen. I would like to acknowledge the financial support provided by Program for Leading Graduate Schools "Integrative Graduate Education and Research in Green Natural Sciences", MEXT, Japan.

Finally, I would like to thank my family for helping me in many ways.